RF Design and Analysis of a Novel Elliptical Reduced Surface Wave Antenna for Wireless Applications

by

Joshua Roy Jacobs

A thesis submitted to the Graduate Faculty of
Auburn University
in partial fulfillment of the
requirements for the Degree of
Master of Science

Auburn, Alabama
May 14, 2010

Keywords: Shorted Annular Ring Antenna, Shorted Annular Elliptical Patch Antenna, Method of Moments

Approved by:

Michael E. Baginski, Chair, Associate Professor of Electrical and Computer Engineering
Stuart M. Wentworth, Associate Professor of Electrical and Computer Engineering
Lloyd S. Riggs, Professor of Electrical and Computer Engineering

Abstract

The Reduced Surface Wave (RSW) antenna is a relatively new class of microstrip patch antenna. An RSW antenna has the ability to drastically reduce both surface and lateral wave radiation, which leads to an increase in antenna efficiency, a reduction in mutual coupling, and a reduction of edge diffraction and scattering. One specific type of antenna displaying RSW characteristics is the Shorted Annular Elliptical Patch (SAEP) antenna. As a result, the SAEP antenna has shown a great deal of promise for wireless applications and as array elements.

In this research, a novel enhanced bandwidth Shorted Annular Elliptical Patch (SAEP) structure specifically designed for wireless applications is presented. A Method of Moments (MoM) code serves as the basis for the antenna design and analysis. The MoM formulation is based on the Electric Field Integral Equation (EFIE) and Rao-Wilton-Glisson (RWG) basis functions. Bandwidth of the SAEP antenna was enhanced by designing the antenna to resonate over two overlapping frequency bands resulting in a broader operating frequency range.

The prototype design was fabricated on Rogers Duroid board. Input impedance measurements were made using a vector network analyzer, and radiation pattern measurements were done in a compact antenna range.

Acknowledgments

First of all, I would like to express my love to my mother, Deborah, and sister, Lauren. Thanks for your support and encouragement throughout all of my endeavors.

To my advisor, Dr. Michael E. Baginski, thanks for your patience and guidance in the creation of this thesis.

To Dr. Tyler N. Killian and Dr. Sadasiva M. Rao, thanks for your technical advice and willingness to help with my MoM issues. This would have never been completed without your expertise.

To Veneela Ammula, thanks for your help with the FEKO simulation software and antenna measurements.

To Calvin Cutshaw, Joe Haggerty, and Dr. David Beale, thanks for your help with fabrication of the antennas.

To the SMART Fellowship and American Society of Engineering Education, thanks for the financial support that made this graduate work possible.

To my soon-to-be wife Shelley, thanks for patiently listening to all of my complaints during the development of this thesis. You helped me keep my sanity. I love you.

This work is dedicated to my late father Walter Jacobs. I thank God for giving me such a great father. I am sure you would have loved reading this.

Table of Contents

Abstract ii

Acknowledgments iii

List of Figures v

1 Introduction 1

  1.1 Background and Objectives 1

  1.2 Outline/Organization of Thesis 2

2 MoM Code Development 3

  2.1 Combined PEC/Thin Dielectric Code 3

    2.1.1 PEC Formulation 3

    2.1.2 Thin Dielectric Formulation 8

    2.1.3 PEC and Thin Dielectric Combination 15

    2.1.4 Meshing Considerations 17

    2.1.5 Modeling the Probe Feed 18

    2.1.6 Feed Point and Shorting Ring Connections 19

    2.1.7 Calculating Input Impedance 20

    2.1.8 Far Field Radiation Pattern 21

  2.2 Test Cases 23

3 Design and Characteristics of Enhanced Bandwidth SAEP 33

  3.1 Design Procedure 33

  3.2 Experimental Results 41

4 Conclusion 47

Bibliography 49

List of Figures

2.1 RWG basis function description. 6

2.2 Pulse basis function description. 10

2.3 Quantities for when triangles overlap. 14

2.4 Illustration of aspect ratio. 18

2.5 Model of the probe feed as a thin strip. 19

2.6 Three triangle junction edge. 20

2.7 Rectangular microstrip patch antenna dimensions. 23

2.8 Computed microstrip patch antenna return loss. 24

2.9 Radiation patterns of rectangular microstrip patch antenna at resonance. 25

2.10 SAR-RSW dimensions (top view). 26

2.11 SAR cross section. 26

2.12 Computed SAR input impedance. 27

2.13 Radiation patterns of SAR antenna at resonance. 28

2.14 SAEP dimensions (top view). 30

2.15 Computed SAEP input impedance. 30

2.16 Radiation patterns of SAEP antenna at lower resonance. 31

2.17 Radiation patterns of SAEP antenna at upper resonance. 32

3.1 SAR design input impedance 35

3.2 SAR design radiation patterns at 2.09 GHz. 36

3.3 SAEP design input impedance. 38

3.4 Computed radiation patterns of enhanced bandwidth SAEP at lower resonance ($f = 2.09$ GHz). 39

3.5 Computed radiation patterns of enhanced bandwidth SAEP at upper resonance ($f = 2.15$ GHz). 40

3.6 Computed VSWR of SAR and SAEP antenna designs. 41

3.7 Fabricated SAR antenna. 42

3.8 Fabricated SAEP antenna. 43

3.9 Measured and computed VSWR of SAR and SAEP antenna designs. 43

3.10 Measured radiation patterns of enhanced bandwidth SAEP at lower resonance. . 45

3.11 Measured radiation patterns of enhanced bandwidth SAEP at upper resonance. 46

Chapter 1

Introduction

1.1 Background and Objectives

A relatively new class of microstrip patch antennas, known as Reduced Surface Wave (RSW) antennas, has shown a great deal of promise for wireless applications and as array elements [8]. The key feature of the RSW antenna is the ability to drastically reduce both surface and lateral wave radiation. This leads to an increase in antenna efficiency and a reduction in both mutual coupling and edge diffraction and scattering. Therefore, the RSW antenna is ideally suited for situations where a small ground plane or antenna substrate is essential and for array applications.

One favorable RSW design is the Shorted Annular Ring Reduced Surface Wave (SAR-RSW) antenna [4], [11]. The inner radius of the ring determines the operating frequency of the antenna and is shorted to ground; therefore, the inner edge does not radiate. The outer radius is chosen by determining the value at which surface and lateral waves are minimized and functions as a radiating edge. The SAR-RSW antenna operates over a single frequency band whereas the Shorted Annular Elliptical Patch (SAEP) antenna is a dual band structure [7]. Like the SAR-RSW, the inner radius of the patch determines the operating frequency and is shorted to ground, and the outer radius is chosen to minimize surface and lateral wave radiation. The elliptical shape of the inner and outer radii allows the SAEP to resonate on two frequency bands.

In this research a novel enhanced bandwidth SAEP structure specifically designed for wireless applications is presented. A Method of Moments (MoM) code served as the basis for the antenna design and analysis [5]. Bandwidth of the SAEP antenna was enhanced by designing the antenna to resonate over two overlapping frequency bands resulting in a broader operating frequency range. The MoM formulation is based on the Electric Field Integral Equation (EFIE) and Rao-Wilton-Glisson (RWG) basis functions. A commercially available MoM code (FEKO) [13] was also used in the design process to further refine the design and confirm the antenna characteristics. The prototype antenna was fabricated on Rogers Duroid [12] board and radiation pattern measurements taken in an anechoic chamber.

1.2 Outline/Organization of Thesis

The thesis is organized into four chapters. Following the introduction, Chapter 2 discusses the MoM formulation used for the solution of surface current densities on a Perfect Electric Conductor (PEC)/thin dielectric structure. The integral equations for the PEC and thin dielectric are developed, along with integral equations that couple the PEC and thin dielectric. The expansion and testing processes are described and the final form of the resulting linear system is given in matrix form. Several examples of solutions are also included that validate the code's accuracy.

Chapter 3 describes the entire design procedure used for the enhanced bandwidth SAEP antenna. The MoM code is then used to determine the antenna's dimensions and estimate the input impedance and radiation pattern. The chapter continues with a description of the machining techniques used for the antenna fabrication, followed by discussion of the measurement methodology. Measurement results are then presented and compared to the computer simulations.

Chapter 2

MoM Code Development

This chapter provides a discussion of the development of the integral equations that are applicable to a PEC/thin dielectric antenna structure. Solutions for the current densities are developed using a MoM formulation resulting in a linear system of equations in matrix form. Section 2.1 describes the procedure for computing the currents on a PEC/thin dielectric structure. Several test cases are given in Section 2.2 that compare the code's accuracy to known solutions for three types of patch antennas. The examples shown are as follows: a microstrip patch antenna above a finite ground plane, an SAR-RSW antenna above an infinite ground plane, and an SAEP antenna with an infinite ground plane.

2.1 Combined PEC/Thin Dielectric Code

2.1.1 PEC Formulation

Consider a perfect electric conductor (PEC) illuminated by an incident electric field. The total electric field ($\mathbf{E}^t$) is the sum of the incident electric field ($\mathbf{E}^i$) and scattered electric field ($\mathbf{E}^s$).

$$\mathbf{E}^t(\mathbf{r}) = \mathbf{E}^i(\mathbf{r}) + \mathbf{E}^s(\mathbf{r}) \tag{2.1}$$

Boundary conditions for a PEC state that the total electric field tangential to the surface is zero, therefore

$$\mathbf{E}^i_{\tan}(\mathbf{r}) = -\mathbf{E}^s_{\tan}(\mathbf{r}),\ \mathbf{r} \in S_c \tag{2.2}$$

where S_c is the surface of the conductor, and the vector $\mathbf{r}$ is a position vector to observation points from a global coordinate origin.

The scattered field is then related to the PEC magnetic vector potential $\mathbf{A}_c$ and scalar electric potential Φ_c by

$$\mathbf{E}^s(\mathbf{r}) = -j\omega\mathbf{A}_c(\mathbf{r}) - \nabla\Phi_c(\mathbf{r}) \tag{2.3}$$

where the magnetic vector potential $\mathbf{A}_c$ and scalar electric potential Φ_c are defined as

$$\mathbf{A}_c(\mathbf{r}) = \mu \int\limits_{S_c} \mathbf{J}_c(\mathbf{r}')G(\mathbf{r},\mathbf{r}')dS' \tag{2.4}$$

$$\Phi_c(\mathbf{r}) = -\frac{1}{j\omega\varepsilon} \int\limits_{S_c} \nabla\cdot\mathbf{J}_c(\mathbf{r})G(\mathbf{r},\mathbf{r}')dS' \tag{2.5}$$

and

$$G(\mathbf{r},\mathbf{r}') = \frac{e^{-jkR}}{4\pi R} \text{ where } R = |\mathbf{r}-\mathbf{r}'| \tag{2.6}$$

is the free space Green's function. The vector $\mathbf{r}'$ is a position vector to source points from a global coordinate origin.

Substituting (2.3) for the scattered field in (2.2) yields

$$\mathbf{E}^i_{\text{tan}}(\mathbf{r}) = \left[j\omega\mathbf{A}_c(\mathbf{r}) + \nabla\Phi_c(\mathbf{r})\right]_{\text{tan}},\ \mathbf{r}\in S_c \tag{2.7}$$

In order to approximate the current on the PEC, we define a set of basis functions. Each basis function is to be valid only on a non-boundary edge. $\mathbf{f}_n$ is the basis function defined over the $n = 1, ..., N_c$ non-boundary edges on the conductor. If α_n is the unknown coefficient for the current component on each of the conductor non-boundary edges, the total current on the conductor is given as

$$\mathbf{J}_c = \sum_{n=1}^{N_c} \alpha_n \mathbf{f}_n(\mathbf{r}) \tag{2.8}$$

RWG basis functions with triangular patch modeling are used for the conductor. The triangular mesh consists of two planar triangles, T_n^+ and T_n^-, and is illustrated in Fig. 2.1. The edge shared by the two triangles, the n^{th} edge, is referred to as a non-boundary edge, and edges not associated with the n^{th} edge are defined as boundary edges. The vertex of a triangle not associated with the n^{th} edge is referred to as the triangle's free point. The basis function associated with the n^{th} edge is defined as

$$\mathbf{f}_n(\mathbf{r}) = \begin{cases} \frac{l_n}{2A_n^+}\rho_n^+, & \mathbf{r} \in T_n^+ \\ -\frac{l_n}{2A_n^-}\rho_n^-, & \mathbf{r} \in T_n^- \\ 0, & \text{otherwise} \end{cases} \tag{2.9}$$

and the divergence of the basis function is defined as

$$\nabla \cdot \mathbf{f}_n(\mathbf{r}) = \begin{cases} \frac{l_n}{A_n^+}, & \mathbf{r} \in T_n^+ \\ -\frac{l_n}{A_n^-}, & \mathbf{r} \in T_n^- \\ 0, & \text{otherwise} \end{cases} \tag{2.10}$$

where l_n is the length of the n^{th} edge, A_n^+ is the surface area of triangle T_n^+, and A_n^- is the surface area of triangle T_n^-. Vector ρ_n^+ extends from the triangle T_n^+ free point to point $\mathbf{r}'$, and vector ρ_n^- extends from point $\mathbf{r}'$ to the triangle T_n^- free point. Vector $\mathbf{r}_n^{ct\pm}$ is defined from a global coordinate origin to the centroid of triangle $T_n^\pm$, and vector $\rho_n^{ct\pm}$ is defined from the free point to the centroid of triangle $T_n^\pm$.

Substituting (2.8) into (2.7) results in

$$\mathbf{E}^i(\mathbf{r}) = \sum_{n=1}^{N_c} \alpha_n \left[j\omega \mathbf{A}_{c,n}(\mathbf{r}) + \nabla \Phi_{c,n}(\mathbf{r}) \right] \tag{2.11}$$

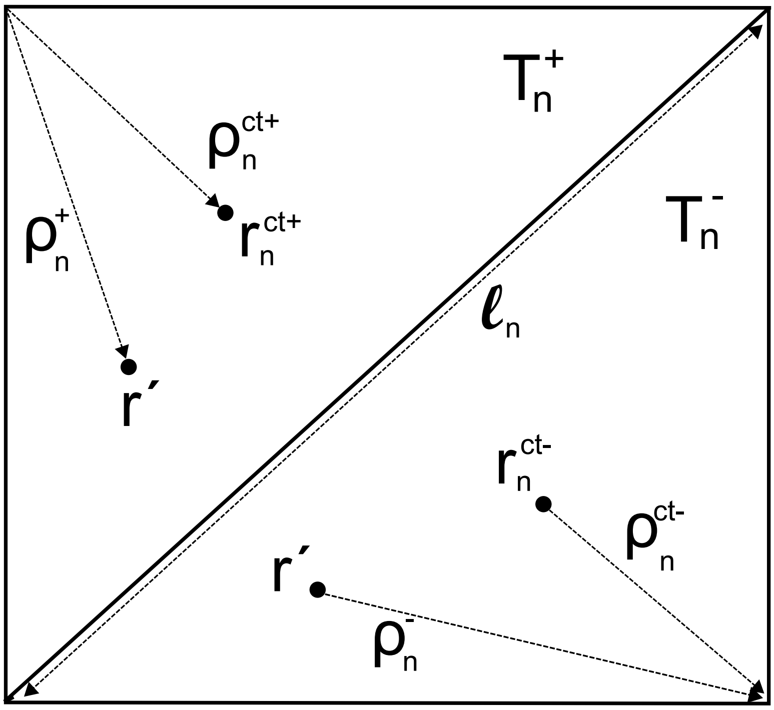

Figure 2.1: RWG basis function description.

where

$$\mathbf{A}_{c,n}(\mathbf{r}) = \mu \int\limits_{S_c} \mathbf{f}_n(\mathbf{r}')G(\mathbf{r},\mathbf{r}')dS' \tag{2.12}$$

$$\Phi_{c,n}(\mathbf{r}) = \frac{-1}{j\omega\varepsilon} \int\limits_{S_c} \nabla \cdot \mathbf{f}_n(\mathbf{r}')G(\mathbf{r},\mathbf{r}')dS' \tag{2.13}$$

The testing procedure is carried out by testing both sides of (2.11) with the same basis function defined in (2.9) that was used for the expansion. This method is known as the Galerkin procedure [2]. The testing procedure uses the inner product as shown below

$$\langle \mathbf{f}, \mathbf{g} \rangle \equiv \int \mathbf{f} \cdot \mathbf{g} dS \tag{2.14}$$

and results in the expression

$$\left\langle \mathbf{E}^i, \mathbf{f}_m \right\rangle = \sum_{n=1}^{N_c} \alpha_n \left[j\omega \left\langle \mathbf{A}_{c,n}, \mathbf{f}_m \right\rangle + \nabla \left\langle \Phi_{c,n}, \mathbf{f}_m \right\rangle \right] \tag{2.15}$$

This will generate a matrix equation of the form

$$[Z_{cc}]\,[I_c] = [V_c] \tag{2.16}$$

where Z_{cc} is a $N \times N$ impedance matrix of moment method elements, I_c is a column vector containing unknown current coefficients, and V_c is a column vector consisting of exitations values for each non-boundary edge defined in the triangular mesh.

The currents on the PEC can be solved for by matrix inversion of (2.16). After testing, the Z matrix is given by

$$Z_{cc,mn} = j\omega \left\langle \mathbf{A}_{c,n}, \mathbf{f}_m \right\rangle + \left\langle \nabla\Phi_{c,n}, \mathbf{f}_m \right\rangle \tag{2.17}$$

The terms defined by testing on the PEC are as follows:

$$\left\langle \mathbf{A}_{c,n}, \mathbf{f}_m \right\rangle = \frac{l_m}{2}\left[\mathbf{A}_{c,n}(\mathbf{r}_m^{ct+}) \cdot \rho_m^{ct+} + \mathbf{A}_{c,n}(\mathbf{r}_m^{ct-}) \cdot \rho_m^{ct-}\right] \tag{2.18}$$

$$\left\langle \nabla\Phi_{c,n}, \mathbf{f}_m \right\rangle = -l_m\left[\Phi_{c,n}(\mathbf{r}_m^{ct+}) - \Phi_{c,n}(\mathbf{r}_m^{ct-})\right] \tag{2.19}$$

The V matrix is given by

$$V_{c,m} = \left\langle \mathbf{E}^i, \mathbf{f}_m \right\rangle \tag{2.20}$$

where

$$\left\langle \mathbf{E}^i, \mathbf{f}_m \right\rangle = \frac{l_m}{2}\left[\mathbf{E}^i(\mathbf{r}_m^{ct+}) \cdot \rho_m^{+} + \mathbf{E}^i(\mathbf{r}_m^{ct-}) \cdot \rho_m^{-}\right] \tag{2.21}$$

This formulation allows one to solve for the currents on any arbitrarily shaped conductor.

2.1.2 Thin Dielectric Formulation

We now consider a dielectric sheet illuminated by an incident electric field. As in the case of the PEC, the total electric field is the sum of the incident electric field and scattered electric field (equation 2.1) and the scattered field is related to the magnetic and scalar potentials by

$$\mathbf{E}^s(\mathbf{r}) = -j\omega\mathbf{A}(\mathbf{r}) - \nabla\Phi(\mathbf{r}) \tag{2.22}$$

where the dielectric magnetic and scalar potentials are

$$\mathbf{A}(\mathbf{r}) = \mu \int\limits_{V_d} \mathbf{J}(\mathbf{r}')G(\mathbf{r},\mathbf{r}')dv' \tag{2.23}$$

$$\Phi(\mathbf{r}) = \frac{-1}{j\omega\varepsilon} \int\limits_{V_d} \nabla\cdot\mathbf{J}(\mathbf{r}')G(\mathbf{r},\mathbf{r}')dv' \tag{2.24}$$

and V_d is the volume of the dielectric.

The dielectric structure can be represented as a set of currents and has a relative permittivity $\varepsilon_r(\mathbf{r})$ at a point $\mathbf{r}$ in the dielectric. The set of polarization currents can then be related to the total electric field by

$$\mathbf{J}(\mathbf{r}) = j\omega\varepsilon_o(\varepsilon_r(\mathbf{r}) - 1)\mathbf{E}^t(\mathbf{r}) = \Omega(\mathbf{r})\mathbf{E}^t(\mathbf{r}) \tag{2.25}$$

where $\Omega(\mathbf{r}) = j\omega\varepsilon_o(\varepsilon_r(\mathbf{r}) - 1)$.

Substituting (2.25) and (2.22) into (2.1) and writing in terms of $\mathbf{A}$ and Φ yields

$$\mathbf{E}^i(\mathbf{r}) = \frac{\mathbf{J}}{\Omega}(\mathbf{r}) + j\omega\mathbf{A}(\mathbf{r}) + \nabla\Phi(\mathbf{r}),\ \mathbf{r} \in V_d \tag{2.26}$$

The total current in the dieletric can be divided into tangential $\mathbf{J}_p$ and normal $\mathbf{J}_q$ components. The tangential and normal currents are with respect to the surface of the dielectric. There are two different basis functions are used to represent the tangential and normal current components. $\mathbf{P}_n$ is the basis function defined over the $n = 1, ..., N_p$ non-boundary and boundary edges in the dielectric, and $\mathbf{Q}_n$ is the basis function over the $n = 1, ..., N_q$ triangles in the dielectric. $\mathbf{P}_n$ and $\mathbf{Q}_n$ represent the basis functions for the tangential and normal components of the dielectric currents, respectively. The total current on the dielectric is now defined as

$$\mathbf{J} = \mathbf{J}_p + \mathbf{J}_q \cong \sum_{n=1}^{N_p} \gamma_n \mathbf{P}_n + \sum_{n=1}^{N_q} \beta_n \mathbf{Q}_n \tag{2.27}$$

where γ_n is the unknown coefficient for the current component on the n^{th} edge in the dielectric, and β_n is the unknown coefficient for the current component in the n^{th} triangle in the dielectric.

The mesh for the dielectric, like that of the PEC, is triangular, so modified RWG basis functions can be used for the tangential current. For non-boundary and boundary edges, the definition of the basis function is as follows:

$$\mathbf{P}_{n,non-boundary}(\mathbf{r}) = \begin{cases} \left(\frac{\varepsilon_{r,n}^{+}-1}{\varepsilon_{r,n}^{+}}\right) \frac{l_n}{2A_n^{+}} \rho_n^{+}, & \mathbf{r} \in T_n^{+} \\ \left(\frac{\varepsilon_{r,n}^{-}-1}{\varepsilon_{r,n}^{-}}\right) \frac{l_n}{2A_n^{-}} \rho_n^{-}, & \mathbf{r} \in T_n^{-} \\ 0, & \text{otherwise} \end{cases} \tag{2.28}$$

$$\mathbf{P}_{n,boundary}(\mathbf{r}) = \begin{cases} \left(\frac{\varepsilon_{r,n}-1}{\varepsilon_{r,n}}\right) \frac{l_n}{2A_n} \rho_n, & \mathbf{r} \in T_n \\ 0, & \text{otherwise} \end{cases} \tag{2.29}$$

and the divergence of the non-boundary basis function is

$$\nabla \cdot \mathbf{P}_n = \begin{cases} \left(\frac{\varepsilon_{r,n}^{+}-1}{\varepsilon_{r,n}^{+}}\right) \frac{l_n}{A_n^{+}}, & \mathbf{r} \in T_n^{+} \\ -\left(\frac{\varepsilon_{r,n}^{-}-1}{\varepsilon_{r,n}^{-}}\right) \frac{l_n}{A_n^{-}}, & \mathbf{r} \in T_n^{-} \\ 0, & \text{otherwise} \end{cases} \tag{2.30}$$

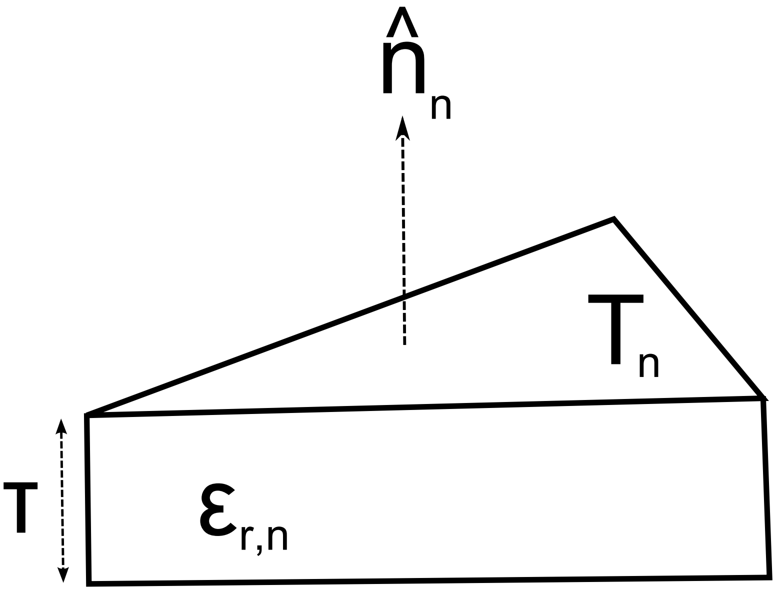

Figure 2.2: Pulse basis function description.

The pulse basis function (illustrated in Fig. 2.2) used for the normal current component is given by

$$\mathbf{Q}_n(\mathbf{r}) = \begin{cases} \hat{n}_n, & \mathbf{r} \in T_n \\ 0, & \text{otherwise} \end{cases} \tag{2.31}$$

where $\hat{n}_n$ is the unit vector normal to the surface of the n^{th} triangle of the dielectric.

Substituting (2.27) into (2.26) yields

$$\mathbf{E}^i = \sum_{n=1}^{N_p} \gamma_n \left(\frac{\mathbf{P}_n}{\Omega} + j\omega \mathbf{A}_{p,n} + \nabla \Phi_{p,n} \right) + \sum_{n=1}^{N_q} \beta_n \left(\frac{\mathbf{Q}_n}{\Omega} + j\omega \mathbf{A}_{q,n} + \nabla \Phi_{q,n} \right) \tag{2.32}$$

where

$$\mathbf{A}_{p,n}(\mathbf{r}) = \mu \int_{V_n} \mathbf{P}_n(\mathbf{r}') G(\mathbf{r}, \mathbf{r}') dv' \tag{2.33}$$

$$\Phi_{p,n}(\mathbf{r}) = \frac{-1}{j\omega\varepsilon} \int\limits_{V_n} \nabla \cdot \mathbf{P}_n(\mathbf{r}')G(\mathbf{r}, \mathbf{r}')dv' \tag{2.34}$$

$$\mathbf{A}_{q,n}(\mathbf{r}) = \mu \int\limits_{V_n} \mathbf{Q}_n(\mathbf{r}')G(\mathbf{r}, \mathbf{r}')dv' \tag{2.35}$$

$$\Phi_{q,n}(\mathbf{r}) = \frac{-1}{j\omega\varepsilon} \int\limits_{V_n} \nabla \cdot \mathbf{Q}_n(\mathbf{r}')G(\mathbf{r}, \mathbf{r}')dv' \tag{2.36}$$

Since the dielectric is thin, the integral equations (2.33), (2.34), and (2.35) are approximated as constant throughout the thickness of the dielectric

$$\mathbf{A}_{p,n}(\mathbf{r}) = \mu\tau \int\limits_{S_n} \mathbf{P}_n(\mathbf{r}')G(\mathbf{r}, \mathbf{r}')dS' \tag{2.37}$$

$$\Phi_{p,n}(\mathbf{r}) = \frac{-\tau}{j\omega\varepsilon} \int\limits_{S_n} \nabla \cdot \mathbf{P}_n(\mathbf{r}')G(\mathbf{r}, \mathbf{r}')dS' \tag{2.38}$$

$$\mathbf{A}_{q,n}(\mathbf{r}) = \mu\tau \int\limits_{S_n} \mathbf{Q}_n(\mathbf{r}')G(\mathbf{r}, \mathbf{r}')dS' \tag{2.39}$$

$$\Phi_{q,n}(\mathbf{r}) = \frac{1}{j\omega\varepsilon} \left[\int\limits_{S_n^+} G(\mathbf{r}, \mathbf{r}')dS' - \int\limits_{S_n^-} G(\mathbf{r}, \mathbf{r}')dS' \right] \tag{2.40}$$

where S_n^+ and S_n^- are the area of the top (in the direction of $\hat{n}_n$) and bottom surfaces, respectively, of triangle T_n in the dielectric.

Galerkin's method is used to complete the testing procedure. This results in a set of linear equations. Both sides of (2.32) are tested with the RWG and pulse basis functions using the inner product as shown

$$\langle \mathbf{f}, \mathbf{g} \rangle \equiv \int \mathbf{f} \cdot \mathbf{g} dS \tag{2.41}$$

and testing yields the following expressions:

$$\begin{aligned}\left\langle \mathbf{E}^i, \mathbf{P}_m \right\rangle &= \sum_{n=1}^{N_p} \gamma_n \left[\frac{1}{\Omega} \left\langle \mathbf{P}_n, \mathbf{P}_m \right\rangle + j\omega \left\langle \mathbf{A}_{p,n}, \mathbf{P}_m \right\rangle + \nabla \left\langle \Phi_{p,n}, \mathbf{P}_m \right\rangle \right] + \\ & \sum_{n=1}^{N_q} \beta_n \left[\frac{1}{\Omega} \left\langle \mathbf{Q}_n, \mathbf{P}_m \right\rangle + j\omega \left\langle \mathbf{A}_{q,n}, \mathbf{P}_m \right\rangle + \nabla \left\langle \Phi_{q,n}, \mathbf{P}_m \right\rangle \right] \end{aligned} \tag{2.42}$$

$$\begin{aligned}\left\langle \mathbf{E}^i, \mathbf{Q}_m \right\rangle &= \sum_{n=1}^{N_p} \gamma_n \left[\frac{1}{\Omega} \left\langle \mathbf{P}_n, \mathbf{Q}_m \right\rangle + j\omega \left\langle \mathbf{A}_{p,n}, \mathbf{Q}_m \right\rangle + \nabla \left\langle \Phi_{p,n}, \mathbf{Q}_m \right\rangle \right] + \\ & \sum_{n=1}^{N_q} \beta_n \left[\frac{1}{\Omega} \left\langle \mathbf{Q}_n, \mathbf{Q}_m \right\rangle + j\omega \left\langle \mathbf{A}_{q,n}, \mathbf{Q}_m \right\rangle + \nabla \left\langle \Phi_{q,n}, \mathbf{Q}_m \right\rangle \right] \end{aligned} \tag{2.43}$$

As a result, the following matrix equation is generated

$$\begin{bmatrix} Z_{pp} & Z_{pq} \\ Z_{qp} & Z_{qq} \end{bmatrix} \begin{bmatrix} I_p \\ I_q \end{bmatrix} = \begin{bmatrix} V_p \\ V_q \end{bmatrix} \tag{2.44}$$

The subscripts in the Z_{pp}, Z_{pq}, Z_{qp}, and Z_{qq} submatrices each denote the coupling between the RWG and pulse basis functions. The exitation from the tangential and normal components in the dielectric are represented by V_p and V_q, respectively. Similarly, I_p and I_q symbolize the tangential and normal components of the current in the dielectric volume.

The Z submatrices are defined as

$$Z_{pp,mn} = \frac{1}{\Omega} \left\langle \mathbf{P}_n, \mathbf{P}_m \right\rangle + j\omega \left\langle \mathbf{A}_{p,n}, \mathbf{P}_m \right\rangle + \left\langle \nabla \Phi_{p,n}, \mathbf{P}_m \right\rangle \tag{2.45}$$

$$Z_{pq,mn} = j\omega \left\langle \mathbf{A}_{q,n} \mathbf{P}_m \right\rangle + \left\langle \nabla \Phi_{q,n}, \mathbf{P}_m \right\rangle \tag{2.46}$$

$$Z_{qp,mn} = j\omega \left\langle \mathbf{A}_{p,n}, \mathbf{Q}_m \right\rangle + \left\langle \nabla\Phi_{p,n}, \mathbf{Q}_m \right\rangle \tag{2.47}$$

$$Z_{qq,mn} = \frac{1}{\Omega} \left\langle \mathbf{Q}_n, \mathbf{Q}_m \right\rangle + j\omega \left\langle \mathbf{A}_{q,n}, \mathbf{Q}_m \right\rangle + \left\langle \nabla\Phi_{q,n}, \mathbf{Q}_m \right\rangle \tag{2.48}$$

The V submatrices are defined as

$$V_{p,m} = \left\langle \mathbf{E}^i, \mathbf{P}_m \right\rangle \tag{2.49}$$

$$V_{q,m} = \left\langle \mathbf{E}^i, \mathbf{Q}_m \right\rangle \tag{2.50}$$

Each of the testing terms in the above equations will now be evaluated. If $\mathbf{P}_m$ and $\mathbf{P}_n$ overlap on triangle T with a relative permittivity ε_r, the following testing term must be evaluated

$$\begin{aligned} \left\langle \mathbf{P}_n, \mathbf{P}_m \right\rangle_T &= \pm \frac{l_n l_m \tau}{4A_m} \left(\frac{\varepsilon_r - 1}{\varepsilon_r} \right) \left[\frac{3\left|\mathbf{r}^{ct}\right|^2}{4} + \frac{\left|\mathbf{r}_1\right|^2 + \left|\mathbf{r}_2\right|^2 + \left|\mathbf{r}_3\right|^2}{12} \right. \\ &\qquad \left. - \left(\mathbf{r}_m + \mathbf{r}_n\right) \cdot \mathbf{r}^{ct} + \mathbf{r}_m \cdot \mathbf{r}_n \right] \end{aligned} \tag{2.51}$$

where $\mathbf{r}^{ct}$ is the centroid vector and $\mathbf{r}_1$, $\mathbf{r}_2$, $\mathbf{r}_3$ are the vectors of the vertices of triangle T with respect to a global coordinate origin. $\mathbf{r}_m$ and $\mathbf{r}_n$ are the vectors of the free points of $\mathbf{P}_m$ and $\mathbf{P}_n$ with respect to a global coordinate origin. If $m = n$ then $\mathbf{P}_m$ and $\mathbf{P}_n$ are associated with an interior, or non-boundary, edge, both T_m^+ and T_m^- will contribute to $\left\langle \mathbf{P}_n, \mathbf{P}_m \right\rangle$. Note that if both basis functions are pointing in the same direction over T, then the sign will be positive. If the basis functions are pointing in opposite directions over T, then the sign will be negative. The quantities in (2.51) are illustrated in Fig. 2.3.

Testing terms for the RWG basis functions are as follows:

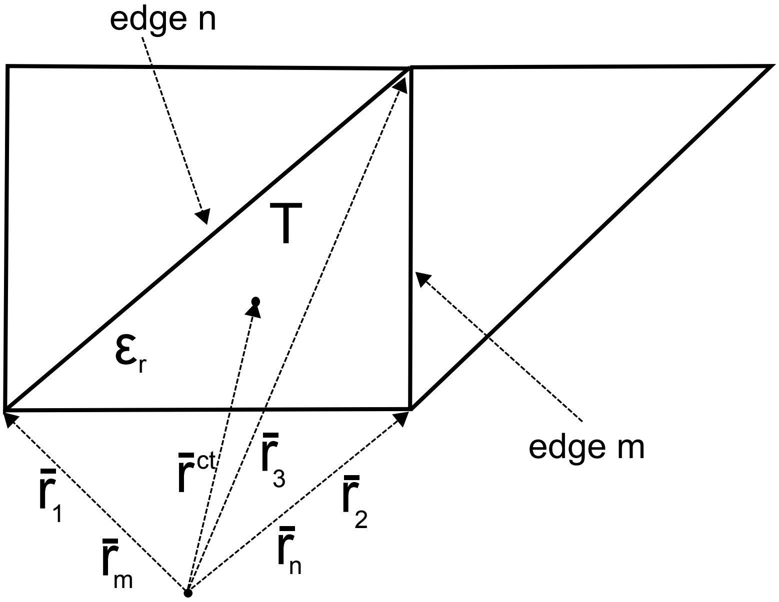

Figure 2.3: Quantities for when triangles overlap.

$$\left\langle \left\{ \begin{array}{c} \mathbf{E}^i \\ \mathbf{A}_{p/q,n} \end{array} \right\}, \mathbf{P}_m \right\rangle = \frac{l_m}{2} \left[\left(\frac{\varepsilon_{r,m}^{+} - 1}{\varepsilon_{r,m}^{+}} \right) \left\{ \begin{array}{c} \mathbf{E}^i(\mathbf{r}_m^{ct+}) \\ \mathbf{A}_{p/q,n}(\mathbf{r}_m^{ct+}) \end{array} \right\} \cdot \rho_m^{ct+} + \left(\frac{\varepsilon_{r,m}^{-} - 1}{\varepsilon_{r,m}^{-}} \right) \left\{ \begin{array}{c} \mathbf{E}^i(\mathbf{r}_m^{ct-}) \\ \mathbf{A}_{p/q,n}(\mathbf{r}_m^{ct-}) \end{array} \right\} \cdot \rho_m^{ct-} \right] \tag{2.52}$$

$$\left\langle \Phi_{p/q,n}, \mathbf{P}_m \right\rangle = -l_m \tau \left[\left(\frac{\varepsilon_{r,m}^{+} - 1}{\varepsilon_{r,m}^{+}} \right) \Phi_{p/q,n}(\mathbf{r}_m^{ct+}) + \left(\frac{\varepsilon_{r,m}^{-} - 1}{\varepsilon_{r,m}^{-}} \right) \Phi_{p/q,n}(\mathbf{r}_m^{ct-}) \right] \tag{2.53}$$

If testing is occuring over a boundary edge, then $\mathbf{P}_m$ is a half RWG basis. A half RWG basis is defined over only one triangle, unlike a normal RWG basis function, which is defined over two triangles. In this situation, the "+" term of the two summation terms in (2.52) and (2.53) are used if the basis function is directed out of T_m, and the "-" term is used otherwise.

The pulse basis function testing terms are defined as

$$\langle \mathbf{Q}_n, \mathbf{Q}_m \rangle = \begin{cases} \frac{\tau A_m}{\Omega}, & if\ n = m \\ 0, & \text{otherwise} \end{cases} \tag{2.54}$$

$$\left\langle \mathbf{A}_{p/q,n}, \mathbf{Q}_m \right\rangle = \tau A_m \mathbf{A}_{p/q,n}(\mathbf{r}_m^{ct}) \cdot \hat{n}_m \tag{2.55}$$

$$\left\langle \nabla\Phi_{p/q,n}, \mathbf{Q}_m \right\rangle = \tau A_m \left(\frac{\Phi_{p/q,n}\left(\mathbf{r}_m^{ct} + 0.25\tau\hat{n}_m\right) - \Phi_{p/q,n}\left(\mathbf{r}_m^{ct} - 0.25\tau\hat{n}_m\right)}{0.5\tau} \right) \tag{2.56}$$

$$\left\langle \mathbf{E}^i, \mathbf{Q}_m \right\rangle = \tau A_m \mathbf{E}^i(\mathbf{r}_m^{ct}) \cdot \hat{n}_m \tag{2.57}$$

This concludes the MoM formulation suitable to calculate currents in a homogeneous or heterogeneous thin dielectric sheet.

2.1.3 PEC and Thin Dielectric Combination

A PEC/thin dielectric structure is now considered. The total magnetic vector potential for the structure is now the sum of the magnetic vector potentials due to the currents on conductor and the tangential and normal current components of the dielectric. The total magnetic vector potential is

$$\mathbf{A} = \mathbf{A}_c + \mathbf{A}_p + \mathbf{A}_q \tag{2.58}$$

where $\mathbf{A}_c$, $\mathbf{A}_p$, and $\mathbf{A}_q$ are magnetic vector potentials due to currents on the conductor and the tangential and normal components of the currents in the dielectric, respectively.

Similarly, the total scalar potential is

$$\Phi = \Phi_c + \Phi_p + \Phi_q \tag{2.59}$$

where Φ_c, Φ_p , and Φ_q are scalar potentials due to currents on the conductor and the tangential and normal components of the currents in the dielectric, respectively.

Substituting (2.8) and (2.27) into (2.58) and (2.59) yields

$$\mathbf{A} = \sum_{n=1}^{N_p} \gamma_n \mathbf{A}_{p,n} + \sum_{n=1}^{N_q} \beta_n \mathbf{A}_{q,n} + \sum_{n=1}^{N_c} \alpha_n \mathbf{A}_{c,n} \tag{2.60}$$

and

$$\Phi = \sum_{n=1}^{N_p} \gamma_n \Phi_{p,n} + \sum_{n=1}^{N_q} \beta_n \Phi_{q,n} + \sum_{n=1}^{N_c} \alpha_n \Phi_{c,n} \tag{2.61}$$

Now, when (2.26) is tested using the Galerkin procedure and the inner product is used, the following matrix equation is generated

$$\begin{bmatrix} Z_{cc} & Z_{cp} & Z_{cq} \\ Z_{pc} & Z_{pp} & Z_{pq} \\ Z_{qc} & Z_{qp} & Z_{qq} \end{bmatrix} \begin{bmatrix} I_c \\ I_p \\ I_q \end{bmatrix} = \begin{bmatrix} V_c \\ V_p \\ V_q \end{bmatrix} \tag{2.62}$$

and can be solved by matrix inversion. Z submatrices Z_{cc}, Z_{pp}, Z_{pq}, Z_{qp}, and Z_{qq} have already been defined. The remaining Z submatrices result from the coupling between the conductor RWG basis functions and the RWG and pulse basis functions in the dielectric are defined as

$$Z_{cp} = j\omega \langle \mathbf{A}_{p,n}, \mathbf{f}_m \rangle + \langle \Phi_{p,n}, \mathbf{f}_m \rangle \tag{2.63}$$

$$Z_{cq} = j\omega \langle \mathbf{A}_{q,n}, \mathbf{f}_m \rangle + \langle \Phi_{q,n}, \mathbf{f}_m \rangle \tag{2.64}$$

$$Z_{pc} = j\omega \langle \mathbf{A}_{c,n}, \mathbf{P}_m \rangle + \langle \Phi_{c,n}, \mathbf{P}_m \rangle \tag{2.65}$$

$$Z_{qc} = j\omega \langle \mathbf{A}_{c,n}, \mathbf{Q}_m \rangle + \langle \Phi_{c,n}, \mathbf{Q}_m \rangle \tag{2.66}$$

where

$$\left\langle \mathbf{A}_{p/q,n}, \mathbf{f}_m \right\rangle = \frac{l_m}{2} \left[\left\{ \mathbf{A}_{p/q,n}(\mathbf{r}_m^{ct+}) \right\} \cdot \rho_m^{ct+} + \left\{ \mathbf{A}_{p/q,n}(\mathbf{r}_m^{ct-}) \right\} \cdot \rho_m^{ct-} \right] \tag{2.67}$$

$$\left\langle \nabla\Phi_{p/q,n}, \mathbf{f}_m \right\rangle = -l_m \left[\Phi_{p/q,n}(\mathbf{r}_m^{ct+}) - \Phi_{p/q,n}(\mathbf{r}_m^{ct-}) \right] \tag{2.68}$$

$$\begin{aligned} \langle \{\mathbf{A}_{c,n}, \mathbf{P}_m\} \rangle &= \frac{l_m}{2} \left[\left(\frac{\varepsilon_{r,m}^{+} - 1}{\varepsilon_{r,m}^{+}} \right) \left\{ \mathbf{A}_{c,n}(\mathbf{r}_m^{ct+}) \right\} \cdot \rho_m^{ct+} \right. \\ &\quad \left. + \left(\frac{\varepsilon_{r,m}^{-} - 1}{\varepsilon_{r,m}^{-}} \right) \left\{ \mathbf{A}_{c,n}(\mathbf{r}_m^{ct-}) \right\} \cdot \rho_m^{ct-} \right] \end{aligned} \tag{2.69}$$

$$\langle \nabla\Phi_{c,n}, \mathbf{P}_m \rangle = -l_m \tau \left[\left(\frac{\varepsilon_{r,m}^{+} - 1}{\varepsilon_{r,m}^{+}} \right) \Phi_{c,n}(\mathbf{r}_m^{ct+}) - \left(\frac{\varepsilon_{r,m}^{-} - 1}{\varepsilon_{r,m}^{-}} \right) \Phi_{c,n}(\mathbf{r}_m^{ct-}) \right] \tag{2.70}$$

$$\langle \mathbf{A}_{c,n}, \mathbf{Q}_m \rangle = \tau A_m \mathbf{A}_{c,n}(\mathbf{r}_m^{ct}) \cdot \hat{n}_m \tag{2.71}$$

$$\langle \nabla\Phi_{c,n}, \mathbf{Q}_m \rangle = \tau A_m \left(\frac{\Phi_{c,n}\left(\mathbf{r}_m^{ct} + 0.25\tau\hat{n}_m\right) - \Phi_{c,n}\left(\mathbf{r}_m^{ct} - 0.25\tau\hat{n}_m\right)}{0.5\tau} \right) \tag{2.72}$$

2.1.4 Meshing Considerations

In order to obtain accurate results, a three dimensional triangular surface mesh must be constructed with maximum edge length limited to $\lambda_g/10$ where

$$\lambda_g = \frac{c}{f\sqrt{\varepsilon_r}} \tag{2.73}$$

where λ_g is the wavelength in the dielectric, c is the speed of light, and ε_r is the relative permittivity of the dielectric. If the mesh contains edges that are greater than $\lambda_g/10$, a poorly conditioned moment method matrix could result. Therefore, when creating a triangular surface mesh for an antenna including a PEC and dielectric, care must be taken to ensure that no edge length exceeds $\lambda_g/10$ [5].

Another mesh consideration is aspect ratio [2]. A triangle with a poor aspect ratio contains small internal angles, or more simply put, the triangles look "thin." A mesh that consists of triangles that have a poor aspect ratio can cause the moment method matrix to be more poorly conditioned. A mesh that is ideally constructed will consist of triangles that are all equilateral. The programmer should attempt to create a mesh that contains triangles with the best aspect ratio possible; however, this is not a realistic possibility. Figures 2.4(a) and 2.4(b) show examples of poor and good aspect ratios.

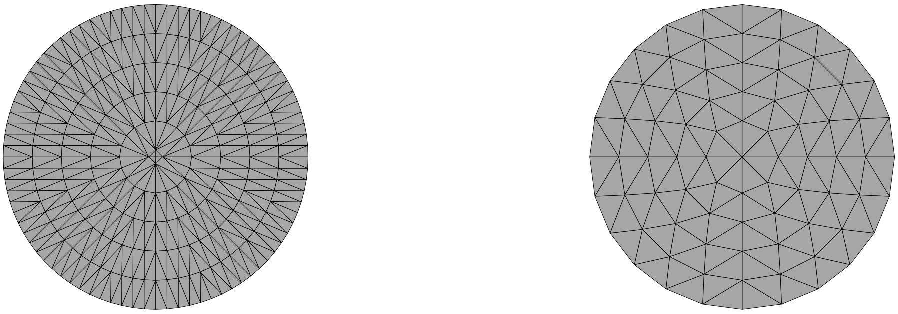

(a) Poor Aspect Ratio

(b) Good Aspect Ratio

Figure 2.4: Illustration of aspect ratio.

2.1.5 Modeling the Probe Feed

One option of feeding a microstrip patch antenna is by using the coaxial probe feed method. Here the outer coaxial conductor is soldered to the back side of the ground plane and the inner cylindrical conductor is fed through the dielectric material and attached to the conducting patch. Since triangular meshing is used, it is convenient to model the inner conductor as a thin strip [1] as illustrated in Fig. 2.5. The width of the strip is given as

$$a = 0.25s \tag{2.74}$$

where a is the radius of the conducting probe, and s is the width of the strip.

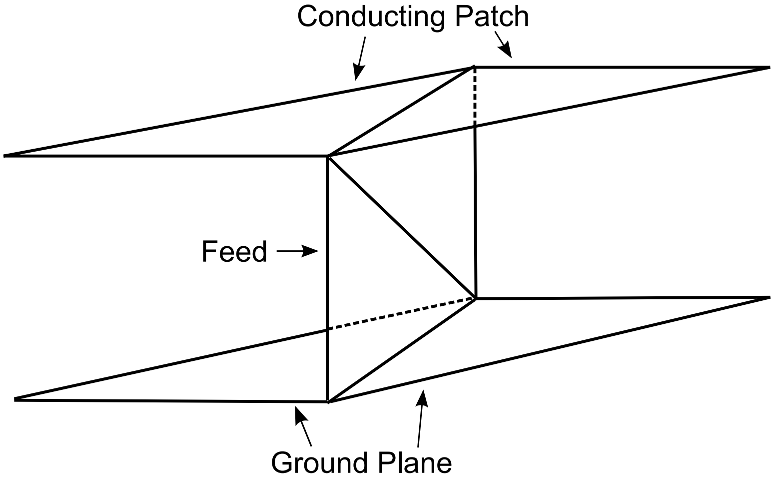

Figure 2.5: Model of the probe feed as a thin strip.

2.1.6 Feed Point and Shorting Ring Connections

An edge connected to three triangles can be associated with three RWG basis function edges. This situation occurs at the ground plane/probe feed junction, conducting patch/probe feed junction, and, in the case of an SAR or SAEP antenna, at the ground plane/shorting ring junction. Despite this, only two basis function edges need to be associated with the junction edge. As illustrated in Fig. 2.6, triangles 1, 2, and 3 are all connected to the junction edge. In this orientation, triangles 1 and 2 represent triangles of the ground plane, and triangle 3 can represent a triangle of the probe feed or shorting ring. An RWG edge element can be created at the junction edge between triangles 1 and 2, between triangles 1 and 3, and between triangles 2 and 3. Since only two edge elements need be used at this junction, only the RWG edge elements sharing triangles 1 and 3 and triangles 2 and 3 need to be utilized. The edge element sharing triangles 1 and 2 can be ignored.

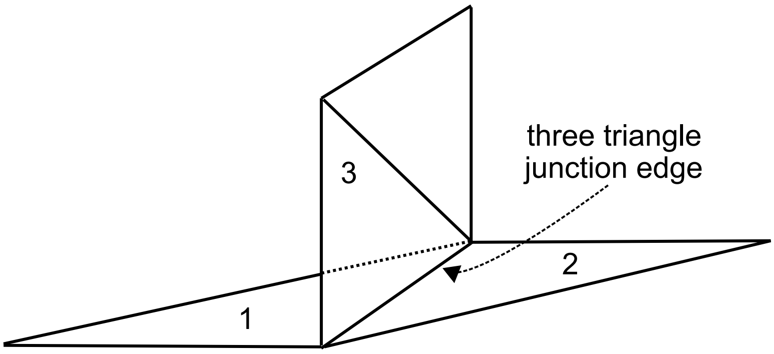

Figure 2.6: Three triangle junction edge.

2.1.7 Calculating Input Impedance

When calculating input impedance, a gap voltage induces the currents on the antenna instead of an incident wave. The delta-gap feed model will be used to supply the voltage applied at the m^{th} edge of the conductor and is given as

$$\mathbf{V}_{c,m} = V l_m \tag{2.75}$$

where l_m is the length of the edge that is being driven. The other entries in $\mathbf{V}$ are set to zero.

The input impedance is defined as

$$Z_{in} = \frac{V}{l_m I_{c,m}} \tag{2.76}$$

where $I_{c,m}$ is the current flowing on the m^{th} edge of the conductor.

Equation (2.76) is suitable for a situation where there is only one RWG element present at the feed edge. In the case of a probe-fed microstrip antenna, the driving edge could consist of two RWG elements as described in Section 2.1.6. The exitation is now

$$V_{c,m_1} = V_{c,m_2} = V l_m \tag{2.77}$$

where the subscripts 1 and 2 denote the two RWG elements associated with the driving edge. Again, the other entries in $\mathbf{V}$ are set to zero.

As a result, the input impedance is given as

$$Z_{in} = \frac{V}{l_m \left(I_{m_1} + I_{m_2}\right)} \tag{2.78}$$

The reflection coefficient is a measure of the impedance mismatch between a transmission line and its load and is calculated by

$$\Gamma_L = \frac{Z_{in} - Z_o}{Z_{in} + Z_o} \tag{2.79}$$

where Z_o is the characteristic impedance of the feed line.

The return loss given in decibels becomes

$$RL = 20 \log |\Gamma_L| \tag{2.80}$$

The voltage standing wave ratio (VSWR), which is a ratio of the maximum to the minimum voltage amplitudes, is related to the reflection coefficient by

$$VSWR = \frac{1 + |\Gamma_L|}{1 - |\Gamma_L|} \tag{2.81}$$

2.1.8 Far Field Radiation Pattern

Determining the currents on the antenna structure allows the scattered far field radiation pattern to be calculated as shown below

$$\mathbf{E}^s = -j\omega\mathbf{A} = -j\omega\mu \int \mathbf{J} \frac{e^{-jkR}}{4\pi R} dv' \tag{2.82}$$

where R can be approximated as

$$R = \mathbf{r} - \hat{\mathbf{r}} \cdot \mathbf{r}' \tag{2.83}$$

and $\hat{\mathbf{r}}$ is the unit vector to observation points from the global point origin. The scattered electric field can now be rewritten as

$$\mathbf{E}^s \approx \frac{-j\omega\mu}{4\pi r} e^{-jkr} \int \mathbf{J} e^{jk\hat{\mathbf{r}}\cdot\mathbf{r}'} dv' \tag{2.84}$$

Equation (2.84) can be used to calculate the far-field contributions from the currents on the conductor $\mathbf{E}_c^s$ as well as the tangential and normal current contributions from the dielectric $\mathbf{E}_p^s$ and $\mathbf{E}_q^s$ respectively as shown below.

$$\mathbf{E}_c^s = \frac{-j\omega\mu}{8\pi r} e^{-jkr} \sum_{n=1}^{N_c} \alpha_n l_n \left[\rho_n^{ct+} e^{jk\hat{\mathbf{r}}\cdot\mathbf{r}_n^{ct+}} + \rho_n^{ct-} e^{jk\hat{\mathbf{r}}\cdot\mathbf{r}_n^{ct-}} \right] \tag{2.85}$$

$$\mathbf{E}_p^s = \frac{-j\omega\mu\tau}{8\pi r} e^{-jkr} \sum_{n=1}^{N_p} \gamma_n l_n \left[\left(\frac{\varepsilon_{r,n}^+ - 1}{\varepsilon_{r,n}^+} \right) \rho_n^{ct+} e^{jk\hat{\mathbf{r}}\cdot\mathbf{r}_n^{ct+}} + \left(\frac{\varepsilon_{r,n}^+ - 1}{\varepsilon_{r,n}^+} \right) \rho_n^{ct-} e^{jk\hat{\mathbf{r}}\cdot\mathbf{r}_n^{ct-}} \right] \tag{2.86}$$

$$\mathbf{E}_q^s = \frac{-j\omega\mu\tau}{8\pi r} e^{-jkr} \sum_{n=1}^{N_q} \beta_n A_n e^{jk\hat{\mathbf{r}}\cdot\mathbf{r}_n^{ct+}} \cdot \hat{n}_n \tag{2.87}$$

The total far field radiation $\mathbf{E}_{total}^s$ is given as

$$\mathbf{E}_{total}^s = \mathbf{E}_c^s + \mathbf{E}_p^s + \mathbf{E}_q^s \tag{2.88}$$

The total radiated electric field $\mathbf{E}^{rad}$ is alway perpendicular to the direction of propagation and is given as

$$\mathbf{E}^{rad} = \mathbf{E}_{total}^s - \left(\mathbf{E}_{total}^s \cdot \hat{\mathbf{r}} \right) \hat{\mathbf{r}} \tag{2.89}$$

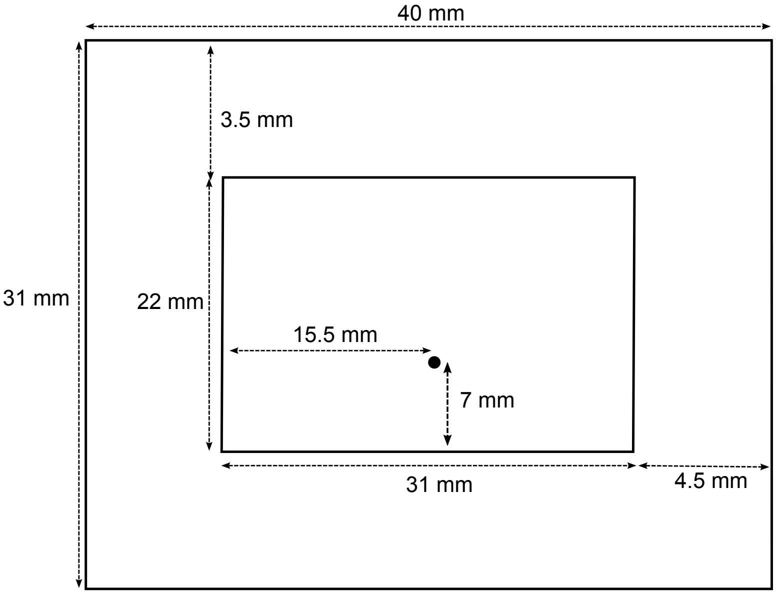

Figure 2.7: Rectangular microstrip patch antenna dimensions.

2.2 Test Cases

This section contains numerical results that demonstrate the accuracy of the PEC/thin dielectric code. The three test case antennas were chosen as follows: a rectangular microstrip patch antenna [6], an SAR-RSW antenna [4], and an SAEP antenna [7].

The rectangular microstrip patch dimensions are shown in Fig. 2.7. The dielectric substrate has a relative permittivity of 11.9 and a thickness of 1.5 mm. Figures 2.8, 2.9(a), and 2.9(b) illustrate the simulated return loss and **E** and **H** plane radiation patterns, respectively, and the results are compared with those given by Nakar [6]. The computed results of the PEC/thin dielectric code show an approximately 5% difference with respect to the results computed by the Zeland IE3D software; however, the computed results show sufficient agreement. The differences in resonant frequency can be possibly explained by differences in the two codes, which could be, but are not limited to basis function selection, meshing strategies, or integration method. The radiation pattern comparison shows good agreement.

The top and cross-sectional view of the SAR-RSW antenna is shown in Fig. 2.10 and Fig. 2.11. The SAR-RSW dimensions are $r_{in} = 2.417$ cm, $r_{out} = 4.392$ cm, and $\rho_{feed} = 2.95$

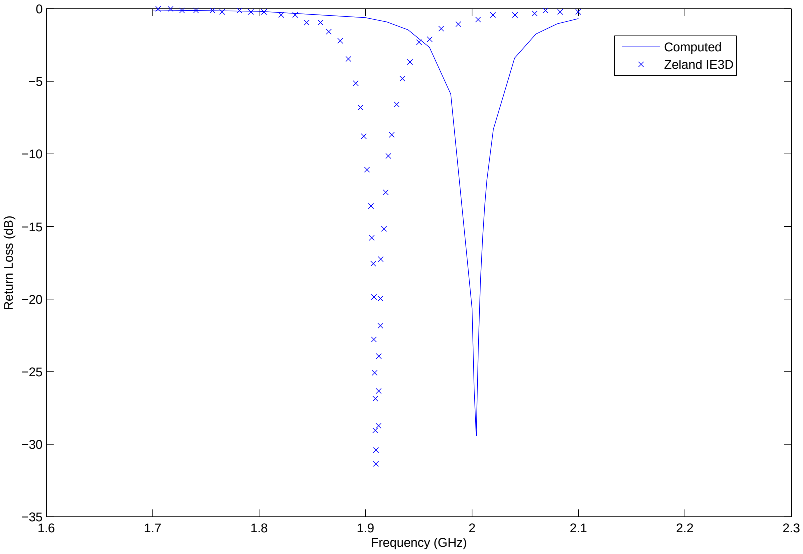

Figure 2.8: Computed microstrip patch antenna return loss.

cm. The probe feed radius is 0.0635 cm. The substrate dielectric constant is 2.94 and thickness is 0.1524 cm. The antenna is simulated on a finite circular ground plane with a radius of 6.588 cm. The antenna in [4] was measured on a 1 m circular ground plane. A comparison of the computed return loss is shown in Fig. 2.12. Fig. 2.13 compares **E** and **H** plane radiation patterns to the results given in [4]. The return loss comparison demonstrates good agreement. The radiation pattern comparison shows good agreement in the main lobe, but poor agreement in the backlobe. The power in the backlobe of the antenna measured in [4] is much lower because the antenna is built on a much larger ground plane. The simulation performed by the PEC/thin dielectric code restricted the ground plane to smaller dimensions because a larger ground plane resulted in to many unknowns.

The geometry for a SAEP antenna is shown in Fig. 2.14. Fig. 2.11 shows a cross section view of the antenna. The SAEP dimensions are $a_{in} = 11.2$ mm, $a_{out} = 1.515$ cm, $b_{in} = 11.1$ mm, and $b_{out} = 1.438$ cm. The input impedance measurements were taken with the feed located at $\rho_{feed} = 12.85$ mm and $\phi = 45°$ with an unspecified ground plane size. The probe feed radius for the input impedance measurements was 0.15 mm. This antenna was

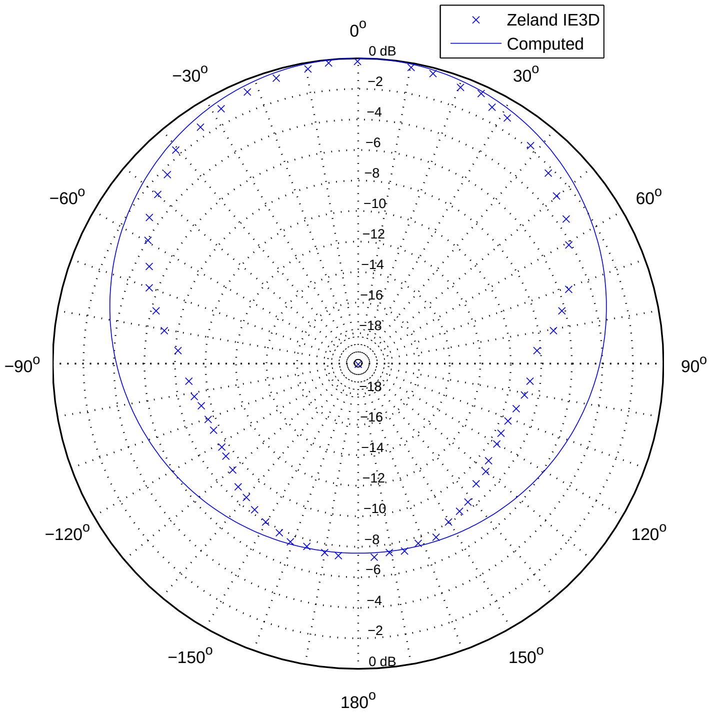

(a) E-plane

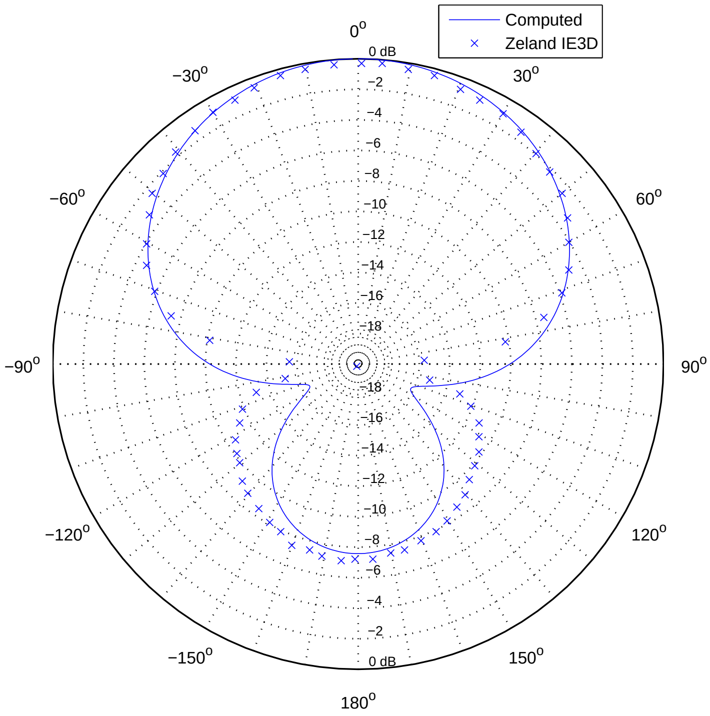

(b) H-plane

Figure 2.9: Radiation patterns of rectangular microstrip patch antenna at resonance.

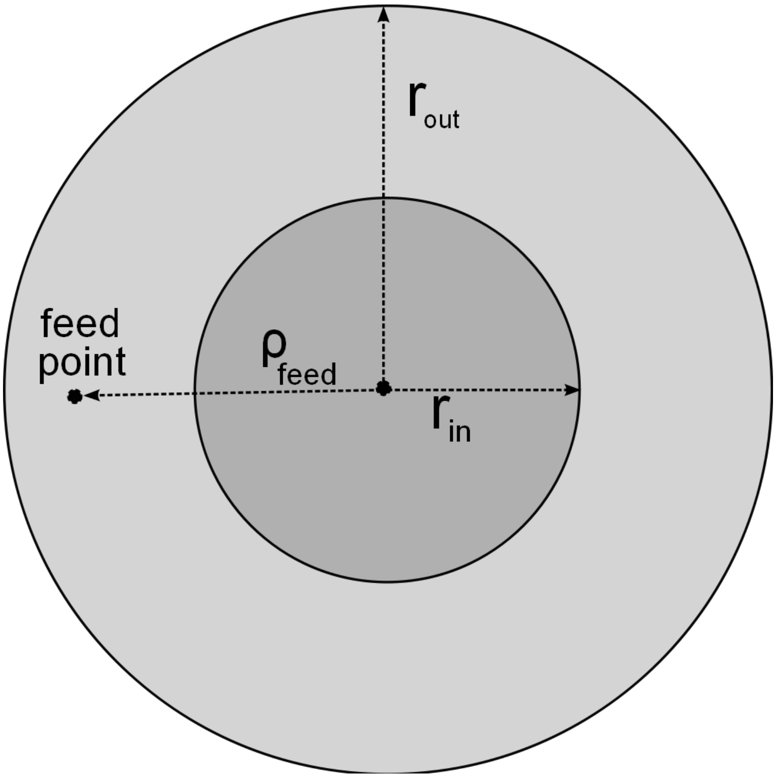

Figure 2.10: SAR-RSW dimensions (top view).

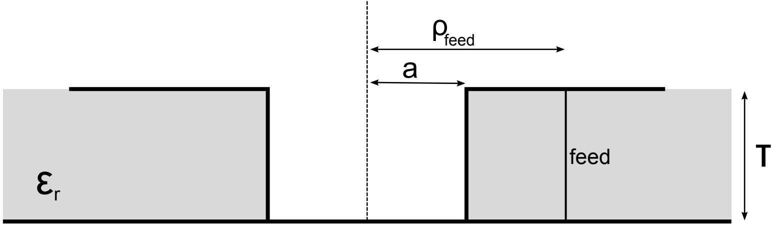

Figure 2.11: SAR cross section.

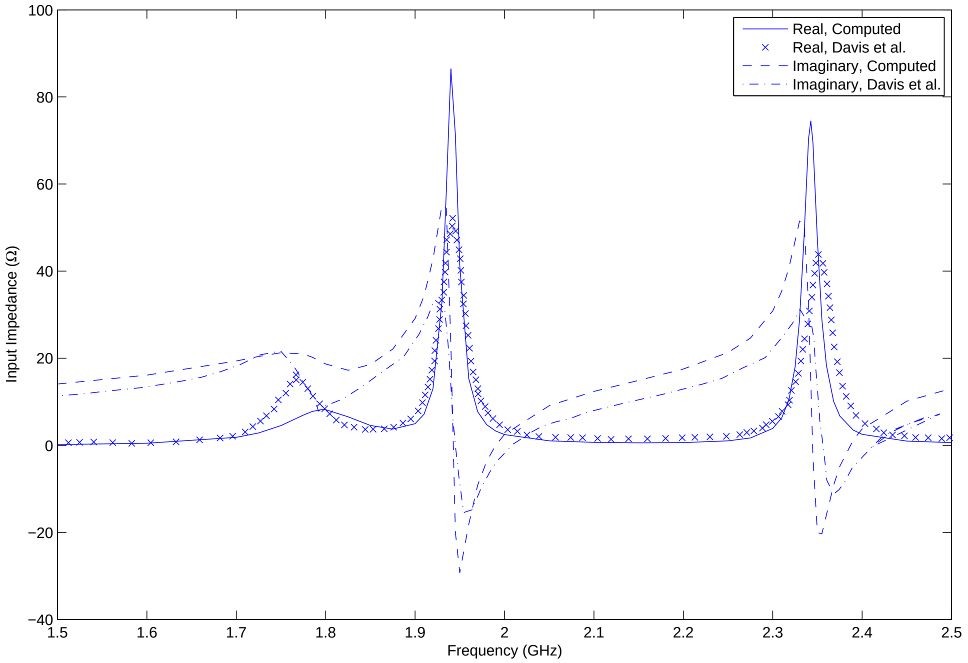

Figure 2.12: Computed SAR input impedance.

simulated on a finite elliptical ground plane where the major axis and minor axis are 1.67 cm and 1.58 cm, respectively. Fig. 2.15 compares the simulated input impedance with the measured input impedance given in [7]. The upper frequency resonance locations differ by approximately 2.2%, the lower frequency resonance locations differ by approximately 1.6%, and the computed input impedance values are higher than those given in [7]. Fabrication error could be the reason for the difference input impedance values because a slight error in feed location can change input impedance values. In [7], the relative permittivity of the dielectric is given, but more detailed information on the substrate is not provided. Perhaps this substrate performs differently at the frequencies studied, resulting in a different relative permittivity. This could change the location of the resonance frequencies. Despite these conditions, the PEC/thin dielectric simulation demonstrates sufficient agreement with the measured results in [7].

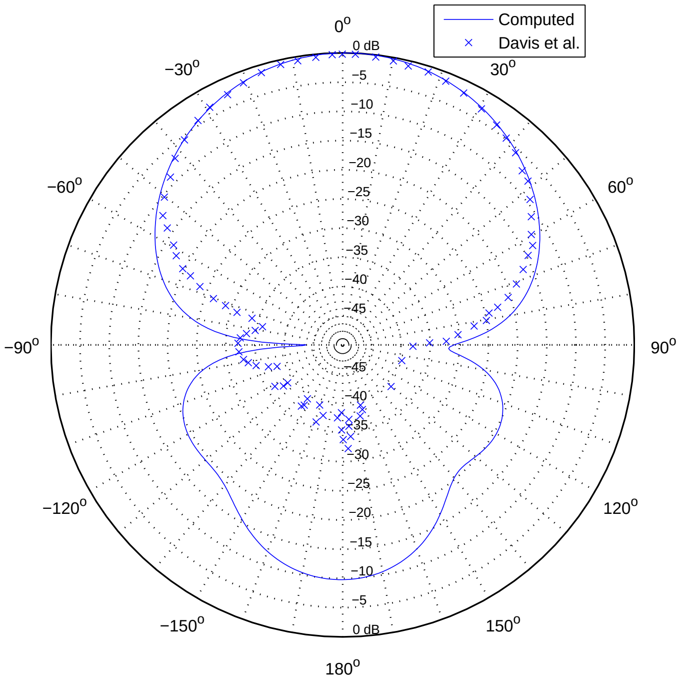

(a) E-plane

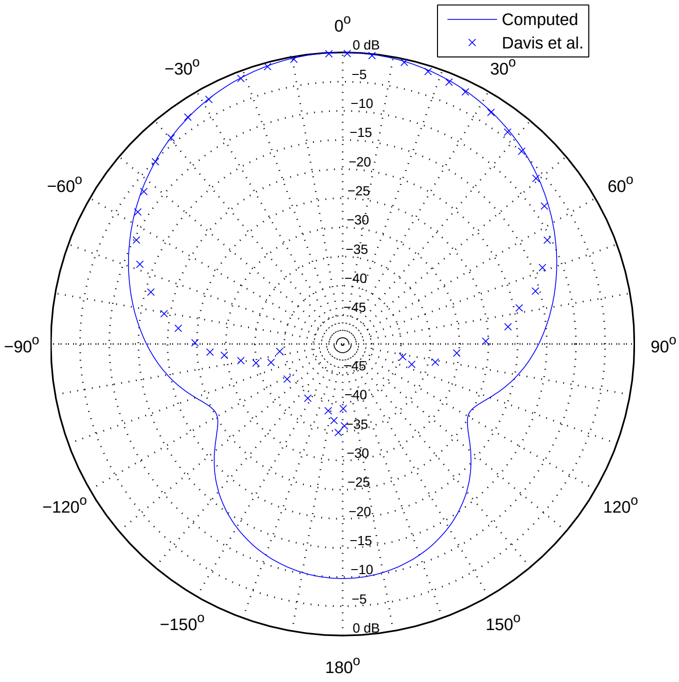

(b) H-plane

Figure 2.13: Radiation patterns of SAR antenna at resonance.

Fig. 2.16 compares the computed **E** and **H** plane radiation patterns of the lower resonance with those illustrated in [7]. This measurement was taken with the feed located at $\rho_{feed} = 13.1$ mm and $\phi = 0°$ in order to excite only the lower frequency resonance of the antenna. As a result the **E**-plane pattern is measured at $\theta = 0° \rightarrow 360°$ and $\phi = 0°$, and the **H**-plane pattern is measured at $\theta = 0° \rightarrow 360°$ and $\phi = 90°$. Fig. 2.17 compares the computed **E** and **H** plane radiation patterns of the upper resonance with those illustrated in [7]. This measurement was taken with the feed located at $\rho_{feed} = 12.95$ mm and $\phi = 90°$ in order to excite only the lower resonance of the antenna. As a result the **E**-plane pattern is measured at $\theta = 0° \rightarrow 360°$ and $\phi = 90°$, and the **H**-plane pattern is measured at $\theta = 0° \rightarrow 360°$ and $\phi = 0°$. The probe feed radius for the pattern measurements was 1 mm. For the substrate, $\varepsilon_r = 10$, and the dielectric thickness is 0.605 mm. The two antennas in [7] were built on a 13 cm × 30 cm grounded dielectric slab and were placed on a metallic plane with a 40 cm radius during measurement. The antennas simulated with the PEC/thin dielectric code was constructed on a finite elliptical ground plane where the major axis and minor axis were 1.67 cm and 1.58 cm, respectively. The computed patterns in Figures 2.16 and 2.17 demonstrate sufficient agreement in the main lobes but poor agreement in the backlobes. As in the SAR-RSW test case, the power in the backlobes of the antennas measured in [7] is much lower because the antenna is built on a much larger ground plane. The simulation performed by the PEC/thin dielectric code restricted the ground plane to smaller dimensions because a larger ground plane resulted in too many unknowns. In addition, large "bumps" are observed at $-90°$ in Fig. 2.16(a) and at $90°$ in Fig. 2.17(a). This is likely due to the fact that the inner conductor radius is not given in [7]. Only the coaxial probe thickness is given, so that value was used to determine the feed probe radius used in the PEC/thin dielectric code. As a result, the feed probe is likely thicker in the simulation than in the fabricated antenna in [7], which would explain why the computed magnitudes of the "bumps" are much larger.

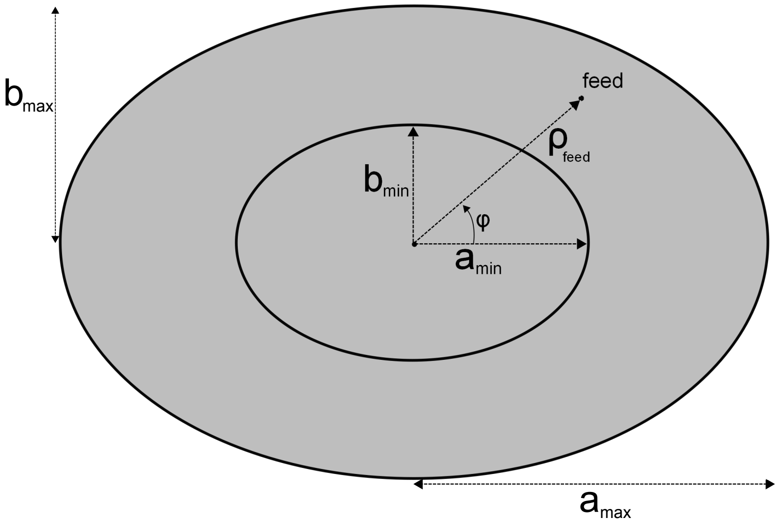

Figure 2.14: SAEP dimensions (top view).

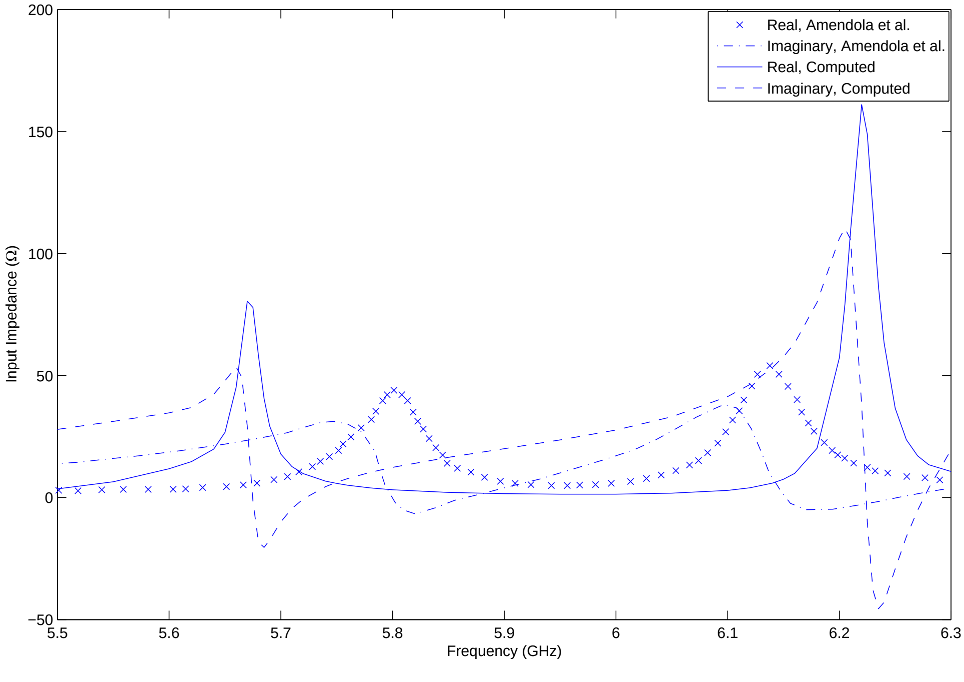

Figure 2.15: Computed SAEP input impedance.

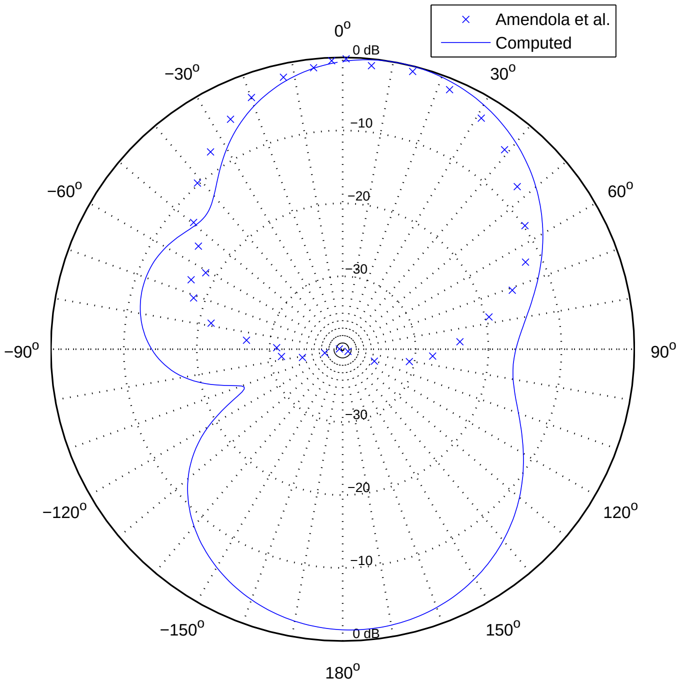

(a) E-plane

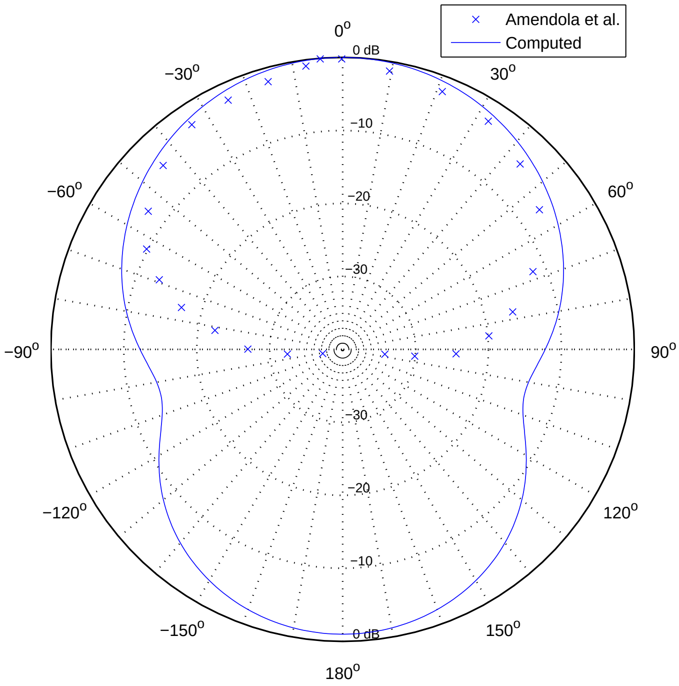

(b) H-plane

Figure 2.16: Radiation patterns of SAEP antenna at lower resonance.

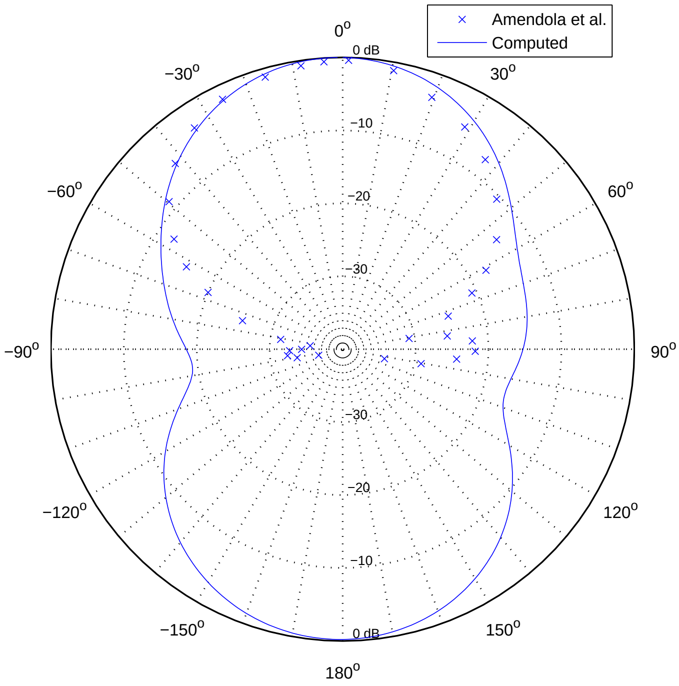

(a) E-plane

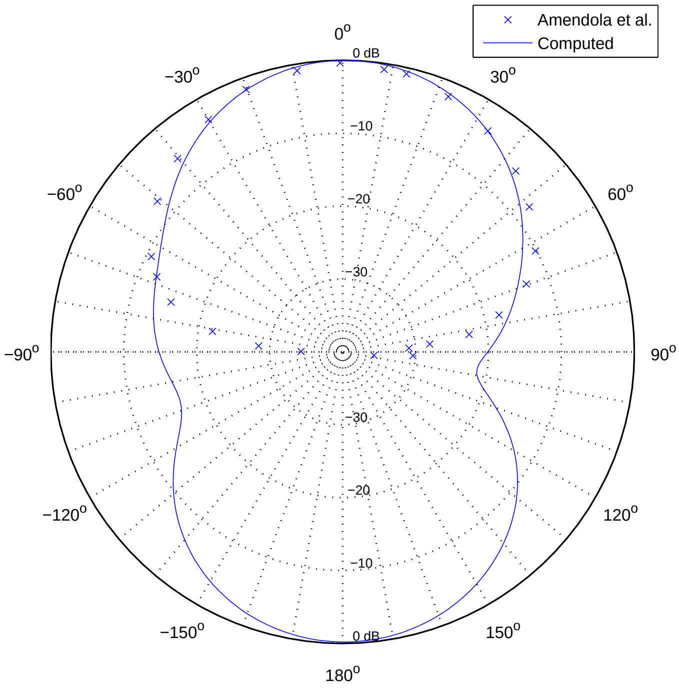

(b) H-plane

Figure 2.17: Radiation patterns of SAEP antenna at upper resonance.

Chapter 3

Design and Characteristics of Enhanced Bandwidth SAEP

This chapter presents the design for an enhanced bandwidth SAEP antenna. In section 3.1, design equations for the SAEP are defined and used to design an SAR antenna only resonating at one frequency. The enhanced bandwidth SAEP antenna is designed by altering the dimensions of the SAR antenna in order to produce two overlapping resonances. Computational results are used to analyze the bandwith of both antennas to demonstrate the bandwidth improvement of the SAEP antenna design.

Section 3.2 describes the fabrication process of the SAR and SAEP antenna designs. The radiation patterns of both antennas are measured in the Auburn University anechoic chamber, and the bandwidth analysis was done by measuring the Voltage Standing Wave Ratio(VSWR) with an HP 8753C vector network analyzer. The results are compared to the PEC/thin dielectric computational results from Section 3.1.

3.1 Design Procedure

In order to design a Shorted Annular Elliptical Patch antenna, we must determine the inner radii for the major and minor axes (a_{min} and b_{min}, respectively) and outer radii for the major and minor axes (a_{max} and b_{max}, respectively) as illustrated in Fig. 2.14. Davis et al. and Amendola et al. state that the inner radius of a shorted annular patch antenna determines the resonant frequency of the antenna, and the outer radius is designed to minimize surface wave radiation.

The entire set of design equations for the SAEP are given in [7], but they were not used because of their complexity. Approximate design equations given in [9] were used as the design starting point and are equivalent to the design equations presented for the Shorted Annular Ring antenna [4] and are found by solving the following:

$$a_{\max} = \frac{1.814}{\beta_{TM_0}} \tag{3.1}$$

and

$$J_1'(ka_{\max})Y_1(ka_{\min}) - Y_1'(ka_{\max})J_1(ka_{\min}) = 0 \tag{3.2}$$

where β_{TM_0} is the surface wave propagation constant, k is the wavenumber in the dielectric, and J_1 and Y_1 are Bessel functions of the first and second kind, respectively, with order $v = 1$. J_1' and Y_1' are derivatives of the aforementioned Bessel functions.

In order to demonstrate that the SAEP design enhances bandwidth relative to the SAR antenna, an SAR antenna was designed first. Since the SAEP antenna resonances must overlap in order to enhance bandwidth, the center frequency of the overlapping resonances is set to be 2 GHz. For a beginning estimate, the lower resonance was set to be 1.975 GHz, and the upper resonance was set at 2.025 GHz. The substrate constitutive parameters were based on Rogers Corporation RT/duroid©5880 high frequency laminate with $\varepsilon_r = 2.2$ and the substrate thickness is 3.175 mm. Here only the SAR case is considered, so the antenna will be designed to resonate on just the lower frequency. Equations (3.1) and (3.2) are solved to determine the inner and outer radii of the SAR antenna illustrated in Fig. 2.10 where a_{min} and a_{max} can be replaced with r_{in} and r_{out}, respectively. The design procedure yields $r_{in} = 23.24$ mm and $r_{out} = 43.85$ mm and the distance from the feed to the origin and feed radius are chosen to be $\rho_{feed} = 27.888$ mm and 0.635 mm, respectively. The design is simulated using both the PEC/thin dielectric code and FEKO simulation software. The PEC/thin dielectric code simulates the antenna over a finite circular ground plane of radius 65.775 mm, but the FEKO simulation is performed using an infinite substrate and ground plane. A comparison of the input impedance results is presented in Fig. 3.1, and a comparison of the **E** and **H** plane radiation patterns is presented in Figures 3.2(a) and

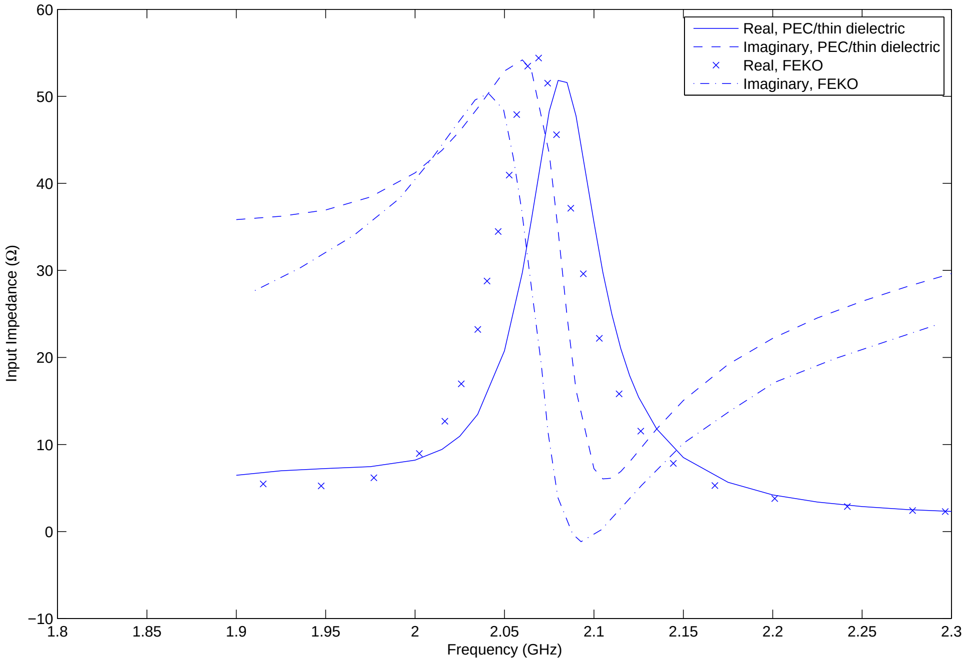

Figure 3.1: SAR design input impedance

3.2(b), respectively. The input impedance comparison shows very good agreement. The radiation pattern comparisons show good agreement in the main lobes, but there are no backlobes shown for the FEKO simulations. This is because the FEKO simulation assumes an infinite ground plane, and the PEC/thin dielectric code can only simulate a finite ground plane. Also note that the design equations yield a resonance near 2.1 GHz instead of the desired resonance frequency of 1.975 GHz.

The SAEP design begins by using the same radii used for the SAR design for a_{min} and a_{max}. This will set the lower frequency. In order to enhance the bandwitch of the SAR antenna, the SAEP antenna resonances must be designed to be close enough to have overlapping bandwidth. Voltage Standing Wave Ratio (VSWR), defined in (2.81), is used to analyze the bandwidth of the antennas. Bandwidth will be defined as $VSWR \leq 2:1$ or better, which is a commonly accepted figure [10]. Rewritting (3.1) and (3.2) in terms of b_{min} and b_{max} allows for the determination of the inner and outer radii of the minor axis of

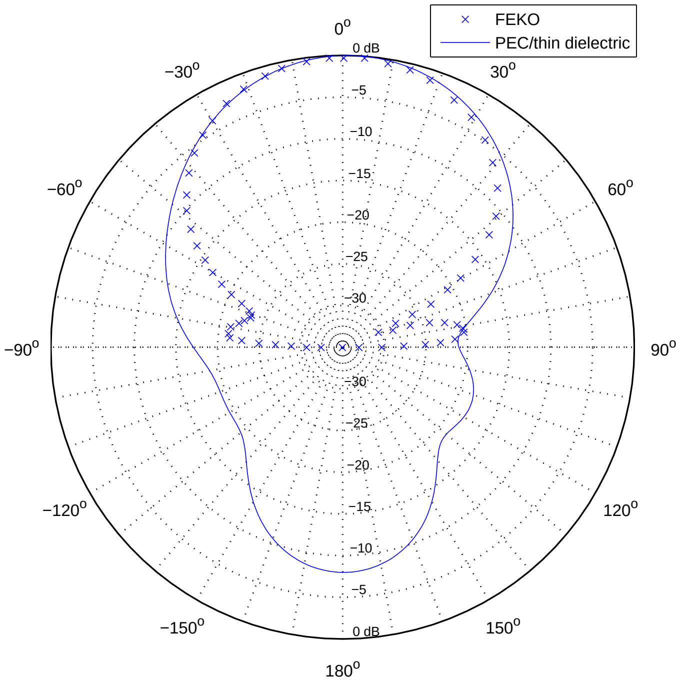

(a) E-plane

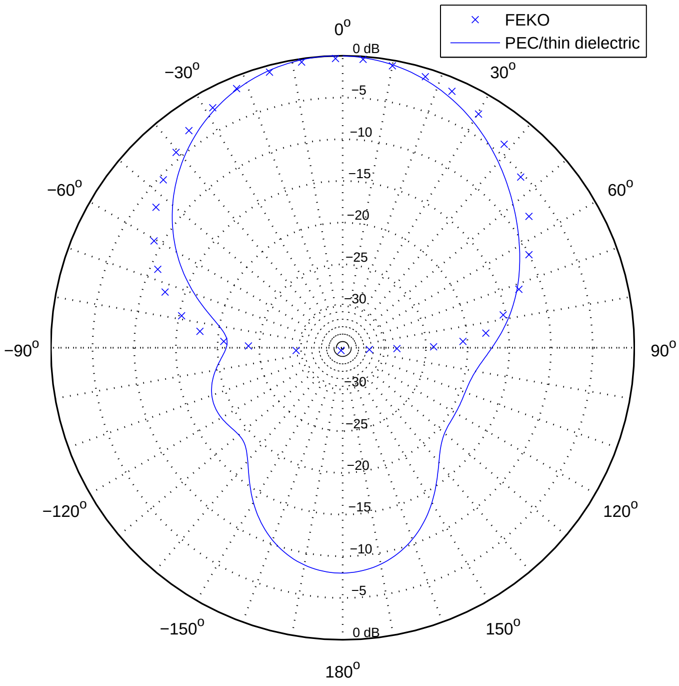

(b) H-plane

Figure 3.2: SAR design radiation patterns at 2.09 GHz.

the ellipse; however, this estimate was revised using FEKO simulation software to optimize the antenna in order to achieve the enhanced bandwidth design criteria because of the noted inaccuracy in the design equations.

The lower resonance of the SAEP will be at the same frequency as the resonance in the SAR, since a_{min} and a_{max} in the SAEP design are equal to r_{in} and r_{out}, respectively, for the SAR design. Using FEKO's Particle Swarm Algorithm (PSO) optimization setting, the upper resonance frequency location was specified, and FEKO determined b_{min} and b_{max} for this criteria. The new SAEP design was simulated to determine if the upper resonance is close enough to the lower resonance to allow for an enhanced bandwidth. After several iterations, the optimization procedure yielded $b_{min} = 21.215$ mm and $b_{max} = 41.403$ mm. ρ_{feed} is chosen to be 28.926 mm, and the feed radius is also chosen to be 0.635 mm. The design was simulated using both the PEC/thin dielectric code and FEKO simulation software. The PEC/thin dielectric code simulates the antenna over a finite elliptical ground plane with a major axis and minor axis of length 65.775 mm and 62.1 mm, respectively. The FEKO simulation is performed using an infinite substrate and ground plane. A comparison of the input impedance calculated using the PEC/thin dielectric code and FEKO is presented in Fig. 3.3, and the results show good agreement. The **E**-plane and **H**-plane results for the lower resonance (2.09 GHz) are compared in Figures 3.4(a) and 3.4(b), respectively. The **E**-plane and **H**-plane results for the upper resonance (2.15 GHz) are compared in Figures 3.5(a) and 3.5(b), respectively. All radiation pattern comparisons show good agreement in the main lobes, but there are no backlobes shown in the FEKO simulations. This is because the FEKO simulation assumes an infinite ground plane, and the PEC/thin dielectric code simulates the antenna over a finite ground plane.

To determine whether the SAEP design enhances the bandwidth relative to the SAR design, a VSWR comparison is performed. This comparison is shown in Fig. 3.6. The relative bandwidth of the antenna is given as

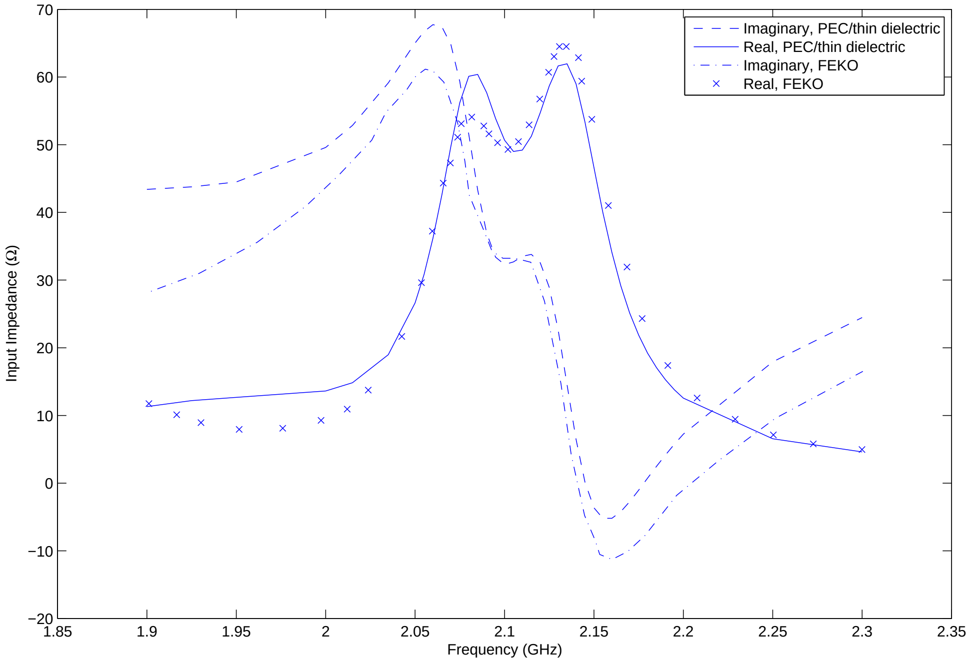

Figure 3.3: SAEP design input impedance.

$$\%BW = \frac{\Delta f}{f_0} \tag{3.3}$$

where Δf is the bandwidth over which $VSWR \leq 2:1$ occurs and f_0 is the center frequency. For the SAR, $\Delta f \approx$ 2.11 GHz - 2.08 GHz = 0.03 GHz and $f_0 = 2.095$ GHz. Using (3.3), percent bandwidth for the SAR is calculated to be 1.43%. For the SAEP, $\Delta f \approx$ 2.17 GHz - 2.09 GHz = 0.08 GHz and $f_0 = 2.125$ GHz. Using (3.3), percent bandwitch for the SAEP is calculated to be 3.76%. Therefore, the SAEP design enhances bandwidth with respect to the SAR design by a remarkable 163%.

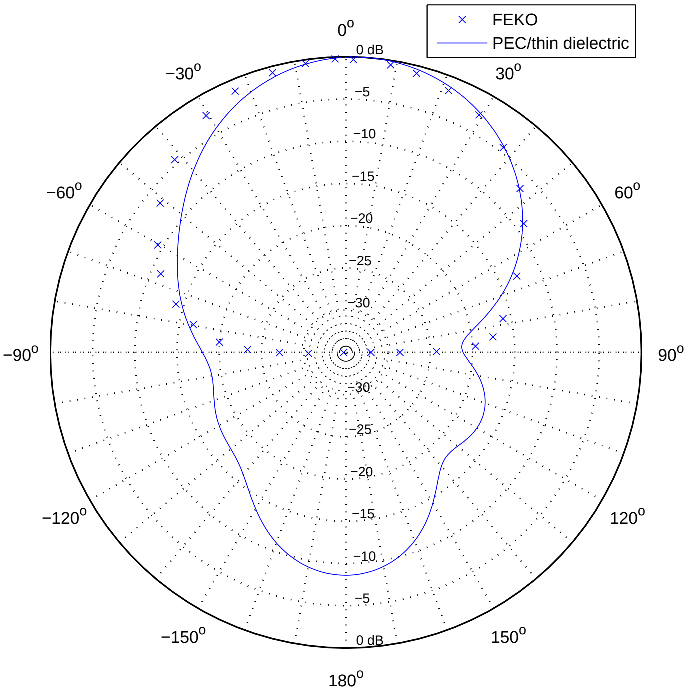

(a) E-plane

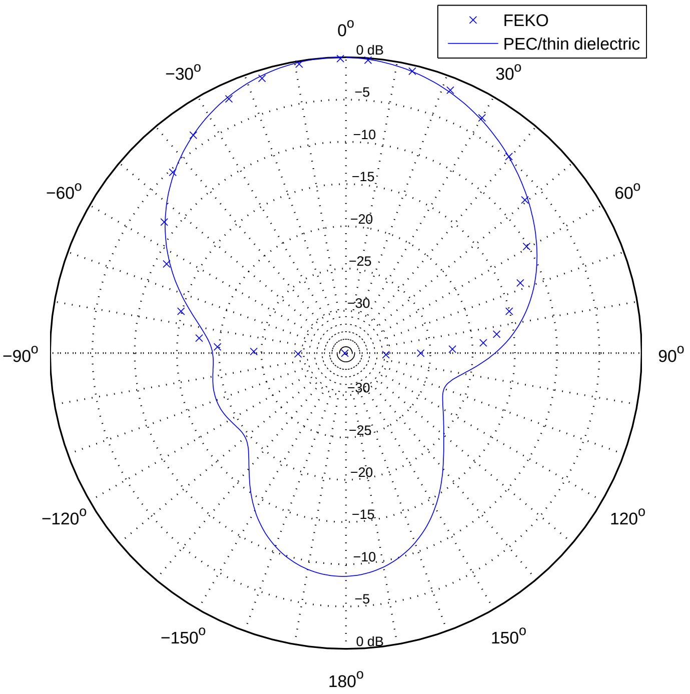

(b) H-plane

Figure 3.4: Computed radiation patterns of enhanced bandwidth SAEP at lower resonance ($f = 2.09$ GHz).

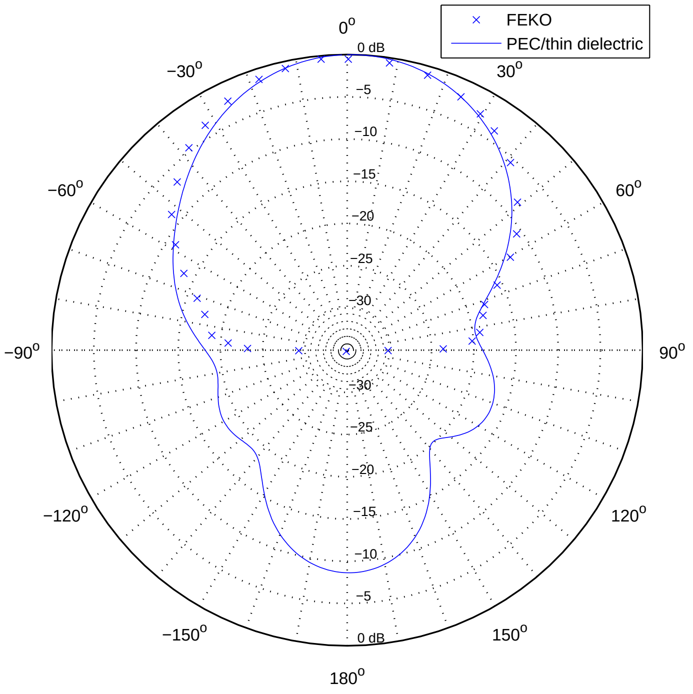

(a) E-plane

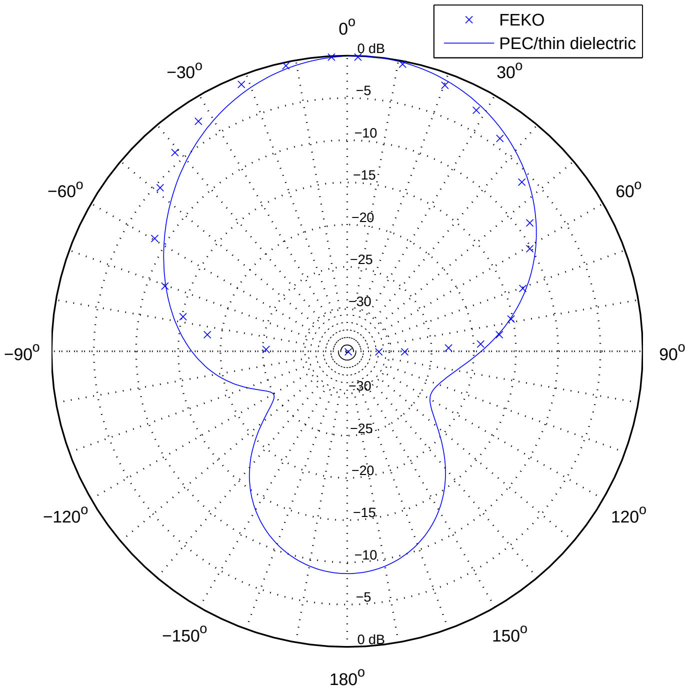

(b) H-plane

Figure 3.5: Computed radiation patterns of enhanced bandwidth SAEP at upper resonance ($f = 2.15$ GHz).

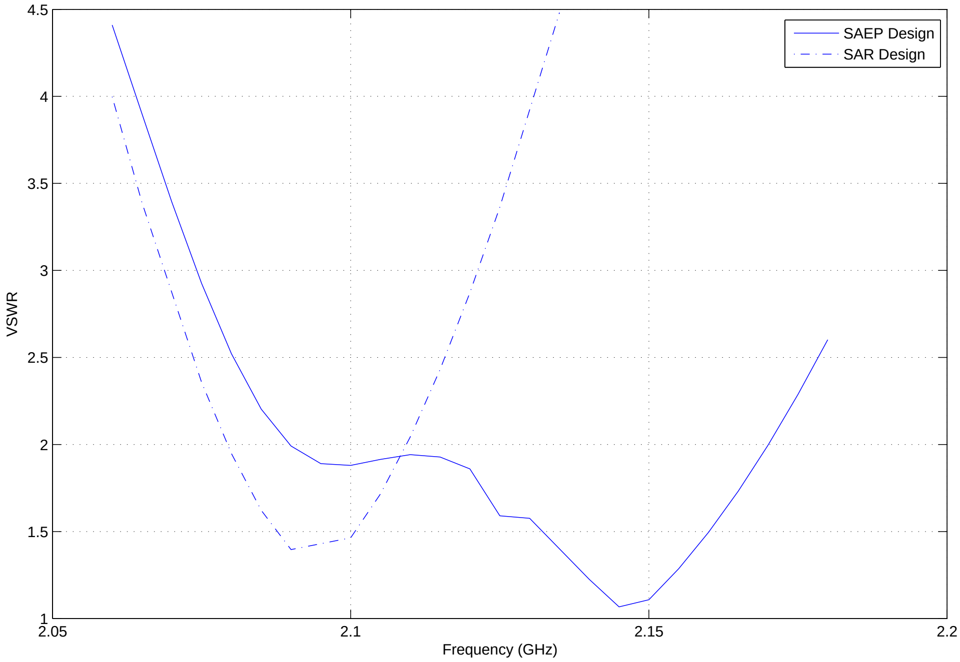

Figure 3.6: Computed VSWR of SAR and SAEP antenna designs.

3.2 Experimental Results

In order to validate the accuracy of the design results of the PEC/thin dielectric code's simulations, the SAR and optimized SAEP antennas designed in the previous section were fabricated. Both antennas were built using Rogers Corporation RT/duroid©5880 high frequency laminate. The area inside the inner radius was drilled completely through the board, and only the top layer of copper was removed beyond the area outside the outer radius. This procedure was performed in the Auburn University Electrical Engineering machine shop for the SAR antenna, and the SAEP antenna was milled by Precision Prototype in Opelika, AL. A hole was drilled at the feed point for each antenna, and an SMA connector was attached. The top conducting patch was shorted to ground using a strip of adhesive copper foil. Finally, a piece of copper foil was soldered to the ground plane in order to cover the hole cut in the ground plane. The SAR antenna was built on a 6 in. x 4.5 in. rectangular ground

Figure 3.7: Fabricated SAR antenna.

plane, and the SAEP was built on a 150 mm x 150 mm square ground plane. A picture of the fabricated SAR and SAEP antennas is shown in Figures 3.7 and 3.8, respectively.

The VSWR of the fabricated SAR and SAEP antennas were analyzed with an HP 8753C vector network analyzer. These results are compared with the simulations conducted with the PEC/thin dielectric code for the SAR and SAEP antennas in Fig. 3.9. Only VSWR results in the operating band of the antennas is shown in Fig. 3.9 to compare their bandwidths. The comparison shows good agreement, although the location of the fabricated SAEP resonance location differs from the simulation results by approximately 2.4%. This small difference is likely due to fabrication error. Using (3.3), the percent bandwidth for the fabricated SAR antenna is 2.39%, and the percent bandwidth for the fabricated SAEP antenna is 5.1%. Therefore, the fabricated SAEP design enhances bandwidth with respect to the fabricated SAR design by 113%.

The radiation patterns of the fabricated SAEP antenna were measured in the Auburn University anechoic chamber. An L-band Scientific Atlanta standard gain horn (SGH 1.7)

Figure 3.8: Fabricated SAEP antenna.

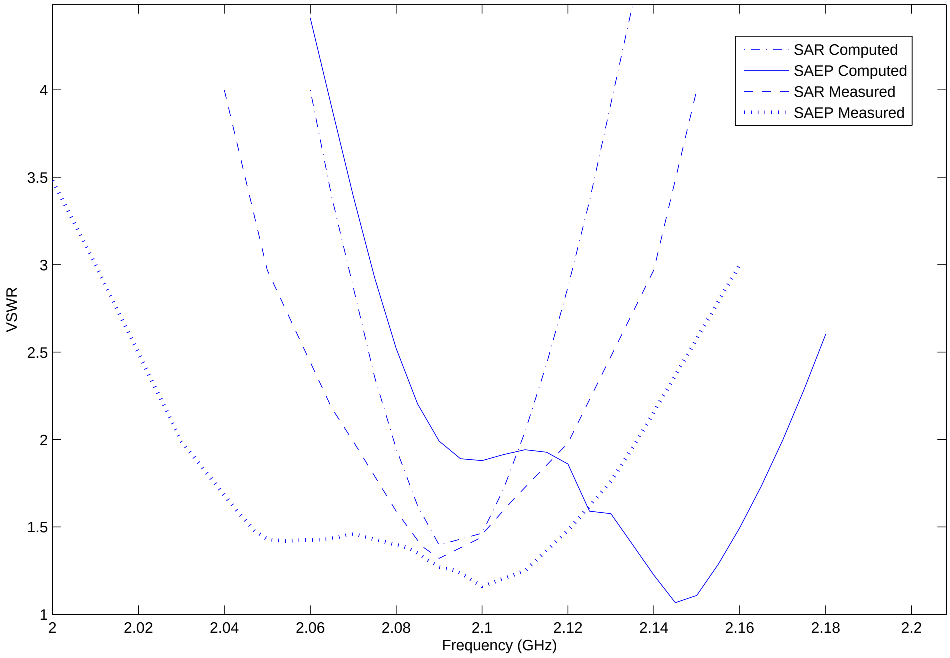

Figure 3.9: Measured and computed VSWR of SAR and SAEP antenna designs.

was used as the source antenna. The source antenna was excited with an HP 8753C vector network analyzer at the lower (2.05 GHz) and upper (2.1 GHz) resonant frequencies of the SAEP antenna. The **E**-plane ($\theta = 0^\circ \rightarrow 360^\circ$, $\phi = 45^\circ$) and **H**-plane ($\theta = 0^\circ \rightarrow 360^\circ$, $\phi = 135^\circ$) pattern cuts were measured using Diamond Engineering's Desktop Antenna Measurement System (DAMS). The radiation patterns for both resonant frequencies are compared with the radiation patterns obtained from the PEC/thin dielectric code computations in Figures 3.10 and 3.11. The radiation pattern comparisons display some differences, which are likely due to different sized ground planes used in the simulations and measurements and fabrication error. Despite these differences, the measurements show sufficient agreement with the simulations.

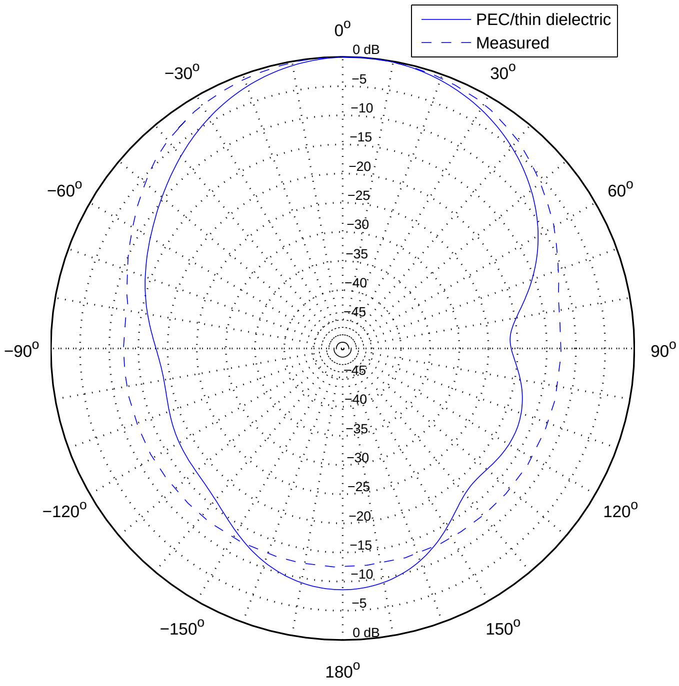

(a) E-plane

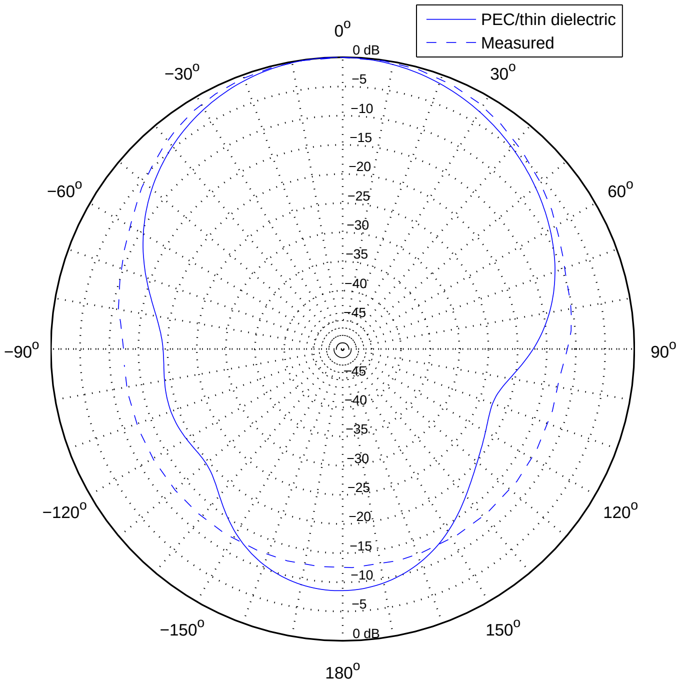

(b) H-plane

Figure 3.10: Measured radiation patterns of enhanced bandwidth SAEP at lower resonance.

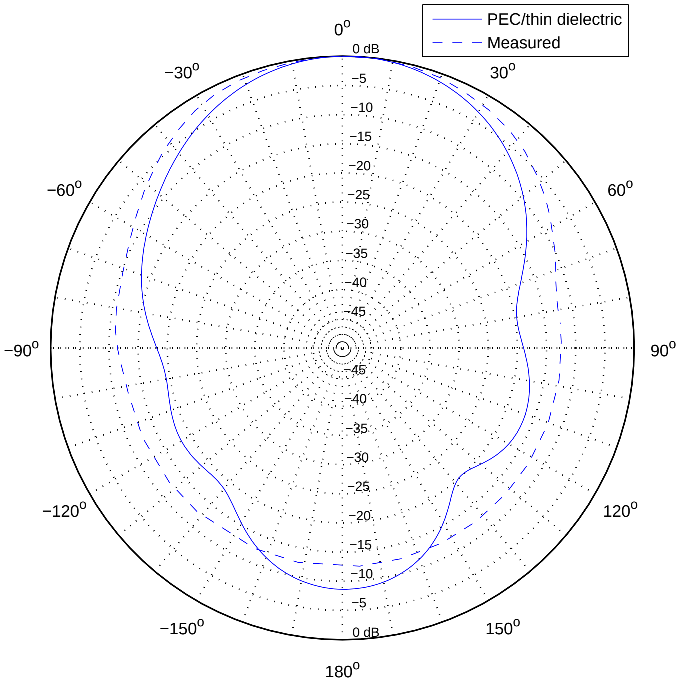

(a) E-plane

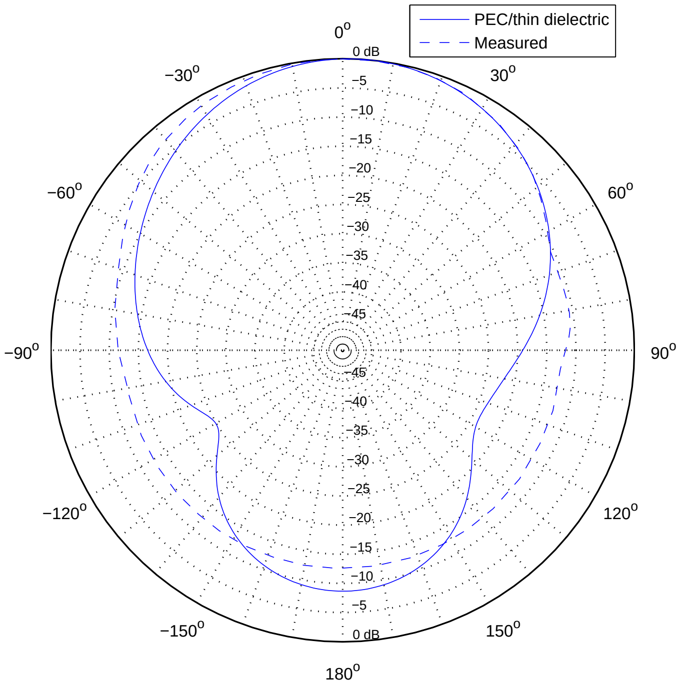

(b) H-plane

Figure 3.11: Measured radiation patterns of enhanced bandwidth SAEP at upper resonance.

Chapter 4

Conclusion

In this work, an enhanced bandwidth Shorted Annular Elliptical Patch antenna was presented. Reduced surface and lateral wave radiation is a key feature of the Shorted Annular Ring antenna, but this geometry only allows for operation at one frequency band. The SAEP design allows for operation in two frequency bands, and this research demonstrates that the two frequency bands can be overlapped so that the bandwidth of the antenna increased in relation to the SAR case by greater than 100%.

In Chapter 2, a computational electromagnetic code was developed to design the enhanced bandwidth SAEP. This Method of Moments code utilized the Electric Field Integral Equation and RWG basis functions to simulate a perfect electric conductor on a thin dielectric sheet. The accuracy of this code was confirmed by comparing the code's computed results with the documented results of a rectangular microstrip patch, SAR, and SAEP antennas. The compared results included return loss, input impedance, and **E**-plane and **H**-plane radiation patterns.

The enhanced bandwidth SAEP antenna was then designed in Chapter 3. The design equations for the SAEP were inaccurate, so because both resonance frequencies for the enhanced bandwidth SAEP needed to be precisely located, FEKO's Particle Swarm Algorithm was used to obtain a more refined and accurate solution. The PEC/thin dielectric code results from the optimized design were compared with FEKO's results and showed good agreement; therefore, the enhanced bandwidth SAEP design was confirmed. Both the SAR and SAEP antennas were built and measurements were taken and compared with the computational results. The bandwidth of the SAEP design was significantly increased compared to the SAR, and the computed and measured radiation patterns displayed good overall agreement.

Future work on this topic would likely focus on improving the PEC/thin dielectric code radiation pattern results. In order to more accurately predict radiation patterns, the code needs to accurately model antennas with large or infinite ground planes. Modeling of an infinite ground plane can be acheived by using image theory. With image theory, the ground plane need not be included in the mesh, resulting in a drastic reduction in the number of unknowns. Also, a more efficient evaluation of the impedance matrix elements by computation of the potential integrals by face-pair combinations, instead of the direct computation of each impedance matrix element used in this work, will reduce the number of integrations required by the code [3]. This improvement would allow faster evaluation of the impedance matrix and reduced memory usage, resulting in an ability for the code to handle problems with a larger number of unknowns.

Bibliography

[1] S. N. Makarov, *Antenna and EM Modeling with MATLAB*, John Wiley & Sons, 2002.

[2] W. C. Gibson, *The Method of Moments in Electromagnetics*, Chapman & Hall/CRC, 2008.

[3] S.M. Rao, D.R. Wilton, and A.W. Glisson, “Electromagnetic Scattering by Surfaces of Arbitrary Shape,” *IEEE Transactions on Antennas and Propagation*, vol. 30, pg 409-418, May 1982.

[4] V. B. Davis, M. A. Khayat, S. Jiang, and D. R. Jackson, “Characteristics of the Shorted-Annular-Ring Reduced-Surface-Wave Antenna,” Department of Electrical and Computer Engineering, University of Houston.

[5] T. N. Killian, “Numerical Modeling of Very Thin Dielectric Materials,” Master of Science Thesis, Auburn University, Aug. 2008.

[6] P.S. Nakar, ”Design of a Compact Microstrip Patch Antenna for Use in Wireless/Cellular Devices,” Master of Science Thesis, Florida State University, 2004.

[7] G. Amendola, L. Boccia, and G. D. Massa, “Shorted Elliptical Patch Antennas With Reduced Surface Waves on Two Frequency Bands,” *IEEE Transactions on Antennas and Propagation*, vol. 53, pg 1946-1956, June 2005.

[8] D. R. Jackson, J. T. Williams, A. K. Bhattacharyya, R. L. Smith, S. J. Buchheit, and S. A. Long, ”Microstrip Patch Designs That Do Not Excite Surface Waves,” *IEEE Transactions on Antennas and Propagation*, vol. 41, pg 1026-1037, Aug. 1993.

[9] L. Boccia, G. Amendola, and G. D. Massa, ”A Shorted Elliptical Patch Antenna for GPS Applications,” *IEEE Antennas and Wireless Propagation Letters*, vol. 2, 2003.

[10] W. L. Stutzman and G. A. Thiele, *Antenna Theory and Design*, John Wiley & Sons, 1998.

[11] M. A. Khayat, J. T. Williams, D. R. Jackson, S. A. Long, ”Mutual Coupling Between Reduced Surface-Wave Microstrip Antennas,” *IEEE Transactions on Antennas and Propagation*, vol. 48, pg 1581-1593, Oct. 2000.

[12] http://www.rogerscorp.com/

[13] http://www.feko.info/